



**Calhoun: The NPS Institutional Archive**  
**DSpace Repository**

---

Theses and Dissertations

1. Thesis and Dissertation Collection, all items

---

2006-06

# Source localization using wireless sensor networks

Tan, Kok Sin Stephen

Monterey California. Naval Postgraduate School

---

<https://hdl.handle.net/10945/2689>

---

*Downloaded from NPS Archive: Calhoun*



Calhoun is the Naval Postgraduate School's public access digital repository for research materials and institutional publications created by the NPS community. Calhoun is named for Professor of Mathematics Guy K. Calhoun, NPS's first appointed -- and published -- scholarly author.

**Dudley Knox Library / Naval Postgraduate School**  
**411 Dyer Road / 1 University Circle**  
**Monterey, California USA 93943**

<http://www.nps.edu/library>



# NAVAL POSTGRADUATE SCHOOL

MONTEREY, CALIFORNIA

## THESIS

### **SOURCE LOCALIZATION USING WIRELESS SENSOR NETWORKS**

by

Tan Kok Sin Stephen

June 2006

Thesis Advisor:  
Co-Advisor:

Murali Tummala  
John McEachen

**Approved for public release, distribution is unlimited**

THIS PAGE INTENTIONALLY LEFT BLANK

<b>REPORT DOCUMENTATION PAGE</b>			<i>Form Approved OMB No. 0704-0188</i>	
Public reporting burden for this collection of information is estimated to average 1 hour per response, including the time for reviewing instruction, searching existing data sources, gathering and maintaining the data needed, and completing and reviewing the collection of information. Send comments regarding this burden estimate or any other aspect of this collection of information, including suggestions for reducing this burden, to Washington headquarters Services, Directorate for Information Operations and Reports, 1215 Jefferson Davis Highway, Suite 1204, Arlington, VA 22202-4302, and to the Office of Management and Budget, Paperwork Reduction Project (0704-0188) Washington DC 20503.				
<b>1. AGENCY USE ONLY (Leave blank)</b>		<b>2. REPORT DATE</b> June 2006	<b>3. REPORT TYPE AND DATES COVERED</b> Master's Thesis	
<b>4. TITLE AND SUBTITLE:</b> Source Localization Using Wireless Sensor Networks			<b>5. FUNDING NUMBERS</b>	
<b>6. AUTHOR(S)</b> Tan Kok Sin Stephen				
<b>7. PERFORMING ORGANIZATION NAME(S) AND ADDRESS(ES)</b> Naval Postgraduate School Monterey, CA 93943-5000			<b>8. PERFORMING ORGANIZATION REPORT NUMBER</b>	
<b>9. SPONSORING /MONITORING AGENCY NAME(S) AND ADDRESS(ES)</b> N/A			<b>10. SPONSORING/MONITORING AGENCY REPORT NUMBER</b>	
<b>11. SUPPLEMENTARY NOTES</b> The views expressed in this thesis are those of the author and do not reflect the official policy or position of the Department of Defense or the U.S. Government.				
<b>12a. DISTRIBUTION / AVAILABILITY STATEMENT</b> Approved for public release, distribution is unlimited			<b>12b. DISTRIBUTION CODE</b>	
<b>13. ABSTRACT (maximum 200 words)</b> Wireless sensors can be worn on soldiers or installed on vehicles to form distributed sensor networks to locate the source of sniper fire. A two-step source localization process is proposed for this sniper detection task. The time difference of arrival (TDOA) for the acoustic signals received by the sensors is first estimated using the generalized cross correlation (GCC) method. The estimated TDOA values are then used by the hybrid spherical interpolation/maximum likelihood (SI/ML) estimation method to estimate the shooter location. A simulation model has been developed in MATLAB to study the performance of the hybrid SI/ML estimation method. A wireless sensor network is simulated in NS-2 to study the network throughput, delay and jitter. Simulation results indicate that the estimation accuracy can be increased by increasing the number of sensors or the inter-sensor spacing. The constraint of small inter-sensor spacing on wearable sensors is found to degrade the estimation accuracy, but vehicular configuration providing larger inter-sensor spacing can help improve the estimation accuracy. The sensor topology should be well represented in all three dimensions to obtain desired estimation accuracy. The estimation accuracy is not adversely affected by sensor node failures or location perturbations. The NS-2 simulation results indicate that the wireless sensor network has low delay and can support fast information exchange needed in counter-sniper applications.				
<b>14. SUBJECT TERMS</b> Wireless sensor networks, source localization, sniper detection, counter-sniper.			<b>15. NUMBER OF PAGES</b> 101	
			<b>16. PRICE CODE</b>	
<b>17. SECURITY CLASSIFICATION OF REPORT</b> Unclassified	<b>18. SECURITY CLASSIFICATION OF THIS PAGE</b> Unclassified	<b>19. SECURITY CLASSIFICATION OF ABSTRACT</b> Unclassified	<b>20. LIMITATION OF ABSTRACT</b> UL	

THIS PAGE INTENTIONALLY LEFT BLANK

**Approved for public release, distribution is unlimited**

**SOURCE LOCALIZATION USING WIRELESS SENSOR NETWORKS**

Tan Kok Sin Stephen  
Civilian, Defence Science and Technology Agency, Singapore  
B.Eng (EE) (Hons)., National University of Singapore, 1997  
M.Eng (EE), National University of Singapore, 1999

Submitted in partial fulfillment of the  
requirements for the degree of

**MASTER OF SCIENCE IN ELECTRICAL ENGINEERING**

from the

**NAVAL POSTGRADUATE SCHOOL  
June 2006**

Author: Tan Kok Sin Stephen

Approved by: Murali Tummala  
Thesis Advisor

John McEachen  
Co-Advisor

Jeffrey B. Knorr  
Chairman, Department of Electrical and Computer Engineering

THIS PAGE INTENTIONALLY LEFT BLANK

## ABSTRACT

Wireless sensors can be worn on soldiers or installed on vehicles to form distributed sensor networks to locate the source of sniper fire. A two-step source localization process is proposed for this sniper detection task. The time difference of arrival (TDOA) for the acoustic signals received by the sensors is first estimated using the generalized cross correlation (GCC) method. The estimated TDOA values are then used by the hybrid spherical interpolation/maximum likelihood (SI/ML) estimation method to estimate the shooter location. A simulation model has been developed in MATLAB to study the performance of the hybrid SI/ML estimation method. A wireless sensor network is simulated in NS-2 to study the network throughput, delay and jitter. Simulation results indicate that the estimation accuracy can be increased by increasing the number of sensors or the inter-sensor spacing. The constraint of small inter-sensor spacing on wearable sensors is found to degrade the estimation accuracy, but vehicular configuration providing larger inter-sensor spacing can help improve the estimation accuracy. The sensor topology should be well represented in all three dimensions to obtain desired estimation accuracy. The estimation accuracy is not adversely affected by sensor node failures or location perturbations. The NS-2 simulation results indicate that the wireless sensor network has low delay and can support fast information exchange needed in counter-sniper applications.



THIS PAGE INTENTIONALLY LEFT BLANK

# TABLE OF CONTENTS

I.	INTRODUCTION.....	1
A.	THESIS OBJECTIVE.....	1
B.	RELATED WORK.....	2
C.	THESIS OUTLINE.....	3
II.	INTRODUCTION TO WIRELESS SENSOR NETWORK, SOURCE LOCALIZATION AND SNIPER DETECTION.....	5
A.	DISTRIBUTED WIRELESS SENSOR NETWORKS .....	5
1.	Architecture.....	5
2.	Standards.....	6
a.	<i>LR-WPAN Architecture</i> .....	7
b.	<i>LR-WPAN Network Topologies</i> .....	8
B.	ACOUSTIC SOURCE LOCALIZATION .....	10
C.	SNIPER DETECTION.....	11
III.	SOURCE LOCALIZATION USING WIRELESS SENSOR NETWORKS .....	13
A.	TWO-STEP LOCALIZATION PROCESS .....	13
1.	Time Difference of Arrival Estimation .....	16
2.	Least-squares Spherical Interpolation (SI) Method .....	17
3.	Maximum Likelihood Estimator .....	20
4.	Cramer Rao Lower Bound.....	21
IV.	SIMULATION RESULTS AND ANALYSIS .....	23
A.	SIMULATION MODEL .....	23
1.	Time Difference of Arrival Estimation .....	24
2.	Hybrid SI/ML Location Estimation.....	24
B.	HYBRID SI/ML ESTIMATION METHOD SIMULATION.....	30
1.	Effect of Number of Sensor Nodes .....	31
2.	Effect of Inter-Sensor Spacing.....	37
a.	<i>Wearable Configuration</i> .....	40
b.	<i>Vehicular Configuration</i> .....	41
3.	Effect of Topology .....	43
4.	Effect of Noise.....	46
5.	Effect of Source-Sensor Distance.....	50
6.	Effect of Node Failures .....	53
7.	Effect of Location Perturbations .....	55
C.	WIRELESS NETWORK SIMULATION .....	56
1.	Sending/Receiving Throughput .....	57
2.	End-to-End Delay.....	59
3.	Packet Size .....	60
4.	Jitter .....	61
V.	CONCLUSION .....	65

A.	SIGNIFICANT RESULTS.....	65
B.	FUTURE WORK.....	66
APPENDIX. MATLAB SOURCE CODE .....		69
LIST OF REFERENCES.....		77
INITIAL DISTRIBUTION LIST .....		79

## LIST OF FIGURES

Figure 1.	Sniper detection and localization using a distributed wireless sensor network. ....	2
Figure 2.	Tiered Architecture in Low Rate Wireless Personal Area Networks (LR-WPAN) (from [7]). ....	6
Figure 3.	IEEE 802.15.4 LR-WPAN device architecture (from [8]). ....	7
Figure 4.	Star and Peer-to-Peer topologies for a IEEE 802.15.4 LR-WPAN (from [8]). ....	9
Figure 5.	IEEE 802.15.4 LR-WPAN cluster tree network (from [8]). ....	9
Figure 6.	Shock wave front and muzzle wave detection by a group of distributed wireless sensors (after [4]). ....	11
Figure 7.	Wireless network-based counter-sniper system consisting of vehicular and wearable sensors. ....	12
Figure 8.	Two-step source localization model using GCC and hybrid SI/ML methods. Step 1 performs the TDOA estimation using GCC; Step 2 performs the location estimation in two stages: estimate determined by SI method in stage 1 is used as initial values for ML method in stage 2. ....	14
Figure 9.	Range difference of arrival at two acoustic sensors. ....	14
Figure 10.	Notations used in Spherical Interpolation (SI) method for a single source, sensor $i$ and the reference sensor 1 (from [13]). ....	18
Figure 11.	Range and bearing estimate of source location. ....	19
Figure 12.	Simulation block diagram for the study of the two-step localization process (based on Figure 8 in Chapter III). ....	23
Figure 13.	Received signals at two sensors. The received signal at sensor 2 is same as the signal received at sensor 1 but is time delayed by $\tau_{12} = 40$ ms. ....	24
Figure 14.	Range difference of arrival $d_{12}$ for a single source, sensor 2 and reference sensor 1 located at $(x_s, y_s, z_s)$ , $(x_2, y_2, z_2)$ and $(0,0,0)$ , respectively. ....	25
Figure 15.	Modeling of range difference of arrival (RDOA). ....	26
Figure 16.	Simulation output of the location estimation using the SI and ML methods in a scenario with the source at 100 m from the origin and the sensors spaced 10 m apart: (a) 24 sensor nodes and (b) 72 sensor nodes. The number of Monte Carlo runs is 100. ....	28
Figure 17.	Schematic of the sensor topology using the three-dimensional XYZ Cartesian coordinate system. White and grey circles represent sensors that are placed in the two-dimensional XY and the three-dimensional XYZ planes, respectively. ....	30
Figure 18.	Effect of number of sensor nodes on the location estimation performance of the hybrid SI/ML method: (a) error mean $\mu$ , (b) error variance $\sigma^2$ , and (c) RMS error $\gamma$ . The readings for 9 and 12 sensors are not shown due to highly erroneous results. Results are based on 100 Monte Carlo runs. ....	33

Figure 19.	Performance of the hybrid SI/ML method for simulated wearable configuration (two sensors per soldier) with different number of soldiers: (a) error mean $\mu$ , (b) error variance $\sigma^2$ , and (c) RMS error $\gamma$ . Results are based on 100 Monte Carlo runs. ....	37
Figure 20.	Effect of inter-sensor spacing on location estimation performance of the hybrid SI/ML method : (a) error mean $\mu$ , (b) error variance $\sigma^2$ , and (c) RMS error $\gamma$ . Results are based on 100 Monte Carlo runs. ....	38
Figure 21.	RMS error $\gamma$ for different values of Z-spacing for $6 \times 2 \times 2$ sensor nodes, representing a wearable configuration. Results are obtained by averaging output from 100 Monte Carlo simulations. ....	41
Figure 22.	RMS error $\gamma$ for different values of Z-spacing, from 1 m to 7 m, representing a vehicular configuration. Results are obtained by averaging output from 100 Monte Carlo simulations. ....	42
Figure 23.	RMS error $\gamma$ for different values of inter-vehicular spacing of 10 m, 20 m, 30 m, and 40 m, representing a vehicular configuration. Results are obtained by averaging output from 100 Monte Carlo simulations. ....	43
Figure 24.	Different sensor topologies: (a) $4 \times 2 \times 1$ , (b) $8 \times 2 \times 1$ , (c) $4 \times 2 \times 2$ and (d) $4 \times 2 \times 3$ . White and grey circles represent sensors that are placed in the two-dimensional $XY$ and three-dimensional $XYZ$ planes, respectively. ....	44
Figure 25.	RMS error $\gamma$ for different two-dimensional ( $4 \times 2 \times 1$ and $8 \times 2 \times 1$ ) and three-dimensional topologies ( $4 \times 2 \times 2$ and $4 \times 2 \times 3$ ). Results are obtained by averaging output from 100 Monte Carlo simulations. ....	45
Figure 26.	RMS error $\gamma$ for two-sensor ( $6 \times 2 \times 2$ with Z-spacing of 1 m and 1.5 m) and three-sensor ( $6 \times 2 \times 3$ with Z-spacing of 0.5 m and 0.75 m) topologies, representing wearable configuration. Results are obtained by averaging output from 100 Monte Carlo simulations. ....	46
Figure 27.	Simulated scenario of 24 sensor nodes ( $6 \times 2 \times 2$ ) with a 10-m spacing between adjacent sensors is simulated. The source is placed 100 m from the origin. ....	47
Figure 28.	Effect of noise on location estimation performance of the hybrid SI/ML method with different noise variance $\sigma_n^2$ for: (a) error mean $\mu$ , (b) error variance $\sigma^2$ , and (c) RMS error $\gamma$ , representing a $6 \times 2 \times 2$ topology. Results are based on 100 Monte Carlo runs. ....	48
Figure 29.	Effect of source-sensor distance on location estimation performance of the hybrid SI/ML method: (a) error mean $\mu$ , (b) error variance $\sigma^2$ , and (c) RMS error $\gamma$ , representing a $6 \times 2 \times 2$ topology. Results are obtained by averaging output from 100 Monte Carlo simulations. Readings for 150 m and beyond are not shown due to erroneous results. ....	51
Figure 30.	RMS error $\gamma$ for different values of source-sensor distances: 50 m, 100 m, 150 m and 200 m, representing a $6 \times 2 \times 2$ wearable configuration. Results are obtained by averaging output from 100 Monte Carlo simulations. ....	53

Figure 31.	RMS error $\gamma$ as the function of the number of sensor node failures, representing a $6 \times 2 \times 2$ wearable configuration. Results are obtained by averaging output from 100 Monte Carlo simulations. ....	54
Figure 32.	RMS error $\gamma$ for different values of standard deviations of location perturbations, representing a $6 \times 2 \times 2$ wearable configuration. ....	55
Figure 33.	The protocol architecture of the IEEE 802.15.4 WPAN extension in NS-2 (from [8]). ....	56
Figure 34.	NS-2 WPAN and WLAN Simulation Scenario: 26 sensor nodes in a $50 \times 50 \text{ m}^2$ area. The Time Interval Length (TIL) used in the simulation is equal to one second. ....	57
Figure 35.	Sending and Receiving Throughput of: (a) WPAN and (b) WLAN. The Time Interval Length (TIL) used in the simulation is equal to one second. NS-2 simulation of a 26-node network operating over an area of $50 \times 50 \text{ m}^2$ . ....	58
Figure 36.	End-to-End delay for: (a) WPAN and (b) WLAN. NS-2 simulation of a 26-node network operating over an area of $50 \times 50 \text{ m}^2$ . ....	60
Figure 37.	Simulation summary statistics for: (a) WPAN and (b) WLAN networks. NS-2 simulation of a 26-node network operating over an area of $50 \times 50 \text{ m}^2$ . ....	61
Figure 38.	Jitter plot of: (a) all sent WPAN packets, (b) all received WPAN packets (c) all sent WLAN packets, (d) all received WLAN packets. NS-2 simulation of a 26-node network operating over an area of $50 \times 50 \text{ m}^2$ . ....	63

THIS PAGE INTENTIONALLY LEFT BLANK

## LIST OF TABLES

Table 1.	IEEE 802.15.4 LR-WPAN frequency bands and data rates (from [8]) .....	8
Table 2.	Mean $\mu$ , variance $\sigma^2$ , and RMS value $\gamma$ of the position errors for the SI and ML methods in a scenario with the source at 100 m from the origin and the sensors spaced 10 m apart. The number of Monte Carlo runs is 100.....	29
Table 3.	Effect of number of sensor nodes on the location estimation performance of the hybrid SI/ML method: error mean $\mu$ , error variance $\sigma^2$ , and RMS error $\gamma$ . The number of Monte Carlo runs is 100.....	34
Table 4.	Effect of inter-sensor spacing on location estimation performance of the hybrid SI/ML method: error mean $\mu$ , error variance $\sigma^2$ , and RMS error $\gamma$ . Results are based on 100 Monte Carlo runs. ....	39
Table 5.	Effect of noise on the location estimation performance of the hybrid SI/ML method with different noise variance $\sigma_n^2$ for: error mean $\mu$ , error variance $\sigma^2$ , and RMS error $\gamma$ , representing a $6 \times 2 \times 2$ topology. Results are obtained by averaging output from 100 Monte Carlo simulations. ....	49
Table 6.	Effect of source-sensor distance on location estimation performance of the hybrid SI/ML method: error mean $\mu$ , error variance $\sigma^2$ , and RMS error $\gamma$ , representing a $6 \times 2 \times 2$ topology. Results are obtained by averaging output from 100 Monte Carlo simulations.....	52



THIS PAGE INTENTIONALLY LEFT BLANK

## **ACKNOWLEDGMENTS**

I would like to express my utmost gratitude to Professor Murali Tummala and Professor John McEachen of the Naval Postgraduate School, Monterey, California for their guidance, patience and contribution to the successful completion of this thesis work.

I also like to thank my family for their constant support and encouragement.

THIS PAGE INTENTIONALLY LEFT BLANK

## EXECUTIVE SUMMARY

In urban warfare, sensor networks can be effectively used to detect, track, and monitor targets of interest. Sniper localization through the collaborative effort of multiple wireless acoustic sensors is of interest in this study. Wireless sensors worn on soldiers or installed on vehicles can be deployed to form a distributed sensor array to locate the source of sniper fire. A two-step source localization process is proposed in this work for counter-sniper applications: the time difference of arrival (TDOA) values are first determined using the generalized cross correlation (GCC) method and then the TDOA values are used by a hybrid spherical interpolation/maximum likelihood (SI/ML) estimation method to determine the shooter location. A simulation model has been developed in MATLAB to study the performance of the hybrid SI/ML estimation method. A wireless sensor network is simulated in NS-2 to study the network throughput, delay and jitter of IEEE WPAN and WLAN networks.

The effects of number of sensor nodes, inter-sensor spacing, topology, noise, source-sensor distance, sensor node failure, location perturbation on the location estimation performance have been studied through MATLAB simulation. Simulation results show that the error variance can be reduced by increasing the number of sensor nodes or the inter-sensor spacing. To increase the location estimation accuracy, the number of sensors as well as the inter-sensor spacing should be increased.

For the case of wearable sensors, the constraint of small inter-sensor spacing on the body degrades the estimation performance. On the other hand, vehicular configuration providing larger vertical and horizontal inter-sensor spacing can help improve the location estimation accuracy. The sensor node topology should be well represented in all three dimensions to obtain desired location estimation performance.

The source location estimation accuracy is not adversely affected by sensor node failures or location perturbations. Results show that sensor node failures lead to a gradual degradation of accuracy and not a sudden total system failure. This demonstrates the advantage of using distributed wireless sensor networks to provide greater system

robustness. It is also observed that location perturbations do not adversely affect the location estimation. This illustrates the flexibility of the network configuration and demonstrates the suitability for potential field deployment.

Network simulation results based on the NS-2 package show that the wireless sensor network can support a throughput between 20 kbps and 100 kbps, a low average delay of less than 10 ms and a low average jitter in the range of 5 ms to 10 ms. These are suitable for fast response network-based sniper detection applications that require low delay and fast data exchange.

## LIST OF SYMBOLS, ACRONYMS, AND/OR ABBREVIATIONS

AOA	angle of arrival
CRB	Cramer Rao Bound
DOA	direction of arrival
GCC	Generalized Cross Correlation
LLC	logical link control
LR-WPAN	Low Rate Wireless Personal Area Network
LS	least-squares
MAC	medium access layer
ML	maximum likelihood
OSI	open systems interconnection
PHAT	phase transform
PHY	physical layer
RD	range difference
RDOA	range difference of arrival
RMS	root mean square
RSS	received signal strength
SI	spherical interpolation
SRP	Steered Response Power
SRP-PHAT	Steered Response Power-Phase Transform
SSCS	service specific convergence sub-layer
TOA	time of arrival
TDOA	time difference of arrival
WLAN	wireless local area network
WPAN	wireless personal area network
$\mu$	error mean
$\sigma^2$	error variance
$\gamma$	RMS error

THIS PAGE INTENTIONALLY LEFT BLANK

## I. INTRODUCTION

Low-cost, low-power, multi-functional wireless sensor networks are becoming readily available. The sensor nodes are small in size and are able to sense, process data, and communicate with each other wirelessly.

Wireless sensor networks have several potential applications, especially in the area of military operations [1][2]. In urban warfare, sensors can be deployed in buildings that have been cleared to prevent reoccupation. Sensors can be used to detect physical phenomena, such as motion, acceleration, acoustic and light, and the collected and processed sensor data can be transmitted through wireless links and displayed on mobile devices carried by soldiers.

In urban warfare, sensor networks can be effectively used to detect, track, and monitor targets of interest. Sniper localization through the collaborative effort of multiple wireless acoustic sensors is of interest in this study. An array of acoustic sensors, microphones or piezoelectric pressure sensors, are deployed to detect and process supersonic shockwaves and muzzle blast produced by the gun shot [3]. The measured acoustic data are further processed using source localization techniques in order to estimate the location of the shooter.

### A. THESIS OBJECTIVE

This thesis focused on source localization using wireless sensor networks. Wireless sensors worn on soldiers or installed on vehicles can be deployed to form a distributed sensor array to locate the source of sniper fire. To improve the accuracy of the source localization, a large number of sensors can be deployed to cover a large area of interest [4]. As illustrated in Figure 1, a distributed wireless sensor network, forming a large array of acoustic sensors, is used to detect and locate sniper fire.

A two-step source localization process is proposed in this work for counter-sniper applications: the time difference of arrival (TDOA) values are first determined using the generalized cross correlation (GCC) method and then the TDOA values are used by a hybrid spherical interpolation/maximum likelihood (SI/ML) estimation method to



determine the shooter location. A simulation model is developed in MATLAB to study the performance of the hybrid SI/ML estimation method. A wireless sensor network is simulated in NS-2 to study the network throughput, delay and jitter of IEEE WPAN and WLAN networks.

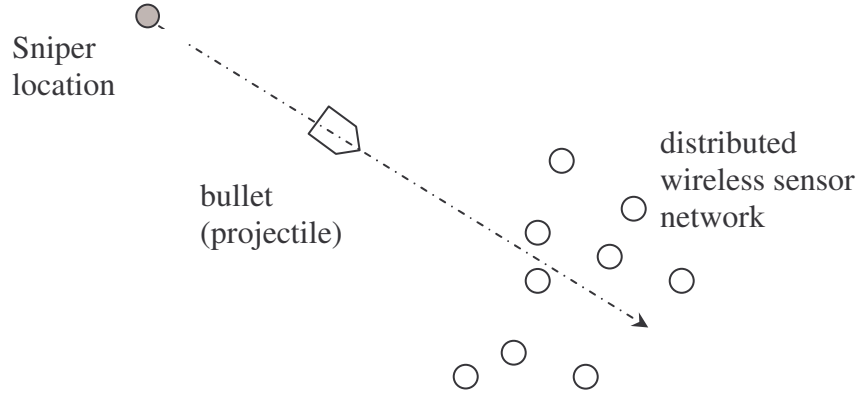


Figure 1. Sniper detection and localization using a distributed wireless sensor network.

## B. RELATED WORK

Several physical phenomena can be used for sniper detection purposes. Pauli et al. have built the VIPER system that utilizes an infrared camera to detect the muzzle flash of the weapon [5]. It is augmented with a microphone to detect the muzzle blast for range estimation. Both sensors require direct line of sight.

Commercial acoustic sniper detection systems, such as BBN's Bullet Ears and Metravib's PILAR, are also based on measurement of the time of arrival (TOA) of muzzle blasts and shockwaves produced by the gun shot. BBN's Bullet Ears system utilizes one or two small arrays of microphones, providing estimates of range to the shooter and the caliber, speed and trajectory of the projectile [6].

Simon et al. have developed an experimental network-based counter-sniper system called PinPtr [4]. The system utilizes an ad hoc wireless sensor network built from inexpensive sensor nodes. After deployment, the sensor nodes synchronize their clocks, perform self-localization and wait for acoustic events. The sensors can detect

muzzle blasts and acoustic shockwaves and measure their time of arrival (TOA). Utilizing a message routing service, the TOA measurements are delivered to a laptop computer, where the sensor signal processing algorithm calculates the shooter location estimate. The proposed solution utilizes time of arrival data of the measured shockwaves and muzzle blasts. From the measurements and the sensor positions a four-dimensional consistency function is formed. A quick search algorithm finds the maximum of this function. The location corresponding to the maximum is the shooter position estimate.

### **C. THESIS OUTLINE**

The organization of the thesis is as follows: chapter II introduces the wireless sensor network as well as the various source localization techniques and sniper detection approaches. Chapter III describes the concept of source localization using wireless sensor networks. The two-step source localization technique proposed for counter-sniper applications will be discussed. Chapter IV presents the simulation model of the two-step source localization process, followed by the simulation results of the hybrid SI/ML estimation method using the MATLAB package simulating a sniper detection scenario. The throughput, delay and jitter of the wireless sensor network are simulated using the NS-2 network simulator. Chapter V concludes the thesis and highlights future work for further investigation. Appendix includes the MATLAB source codes used in the simulation studies.

THIS PAGE INTENTIONALLY LEFT BLANK

## **II. INTRODUCTION TO WIRELESS SENSOR NETWORK, SOURCE LOCALIZATION AND SNIPER DETECTION**

This chapter discusses the various aspects of distributed wireless sensor networks, acoustic source localization and current sniper detection systems. We will introduce the concept of using wireless sensor networks to perform source localization for the purpose of sniper detection.

### **A. DISTRIBUTED WIRELESS SENSOR NETWORKS**

Low-cost, low-power, multi-functional wireless sensor networks are becoming readily available. The wireless sensor nodes are small in size and are able to communicate with each other wirelessly by forming an ad hoc network.

Wireless sensor networks are self-organizing networks with short-range communication and multi-hop routing. Their topologies frequently change due to mobility, fading and node failures. There are usually limitations on transmit power, memory, and computational capability in a sensor node [1].

The performance of a wireless sensor network generally depends on the following factors [1]: energy efficiency, latency, accuracy, fault tolerance, scalability, synchronization and localization, and throughput. Due to the interdependence of energy consumption, delay, and throughput, all these performance issues and metrics are tightly coupled.

For this thesis research, the emphasis is not on any of the above performance metrics. Instead, we will focus on the issue of distributed array processing for determining the location of a signal source of interest.

#### **1. Architecture**

Wireless sensor networks can be organized in two architectures: flat or tiered. In a flat architecture, all sensor nodes are peers and are homogeneous in form and function. However, in a tiered architecture [7], as shown in Figure 2, sensor nodes form a hierarchy in which a sensor node at a given level performs a specific set of tasks on behalf of a subset of sensor nodes in the level below.

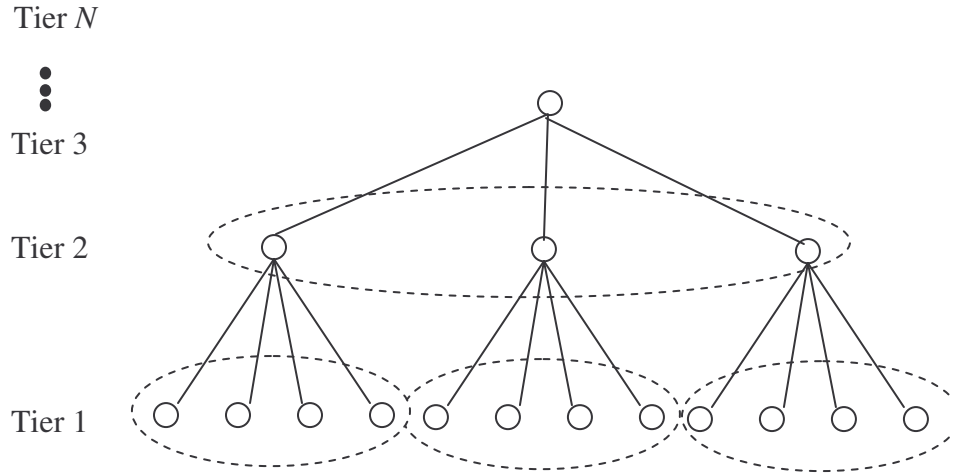


Figure 2. Tiered Architecture in Low Rate Wireless Personal Area Networks (LR-WPAN) (from [7]).

In practice, very few sensor networks are entirely flat. Typically, a sensor network will connect to an internet via gateway nodes. In addition, sensor networks are often not physically homogeneous. For example, a network may become heterogeneous due to uneven battery drain across nodes. Tiered architectures are usually employed to take advantage of unevenly distributed resources by assigning resource-intensive roles to resource-rich nodes.

## 2. Standards

Efforts are under way to standardize the various layers of wireless sensor network communication protocols. IEEE 802.15.4 is the standard defined for Low Rate Wireless Personal Area Networks (LR-WPAN) [8], with the ZigBee Alliance [9] as its marketing and compliance certification organization.

A LR-WPAN is a simple, low-cost communication network that allows wireless connectivity in applications with limited power and relaxed throughput requirements. The main objectives of a LR-WPAN are ease of installation, reliable data transfer, short-range operation, low cost, and a reasonable battery life, while maintaining a simple and flexible protocol suite.

*a. LR-WPAN Architecture*

The LR-WPAN architecture is specified in terms of a number of layers based on the open systems interconnection (OSI) seven-layer model, as shown in Figure 3. Each layer is responsible for one part of the standard and offers services to higher layers.

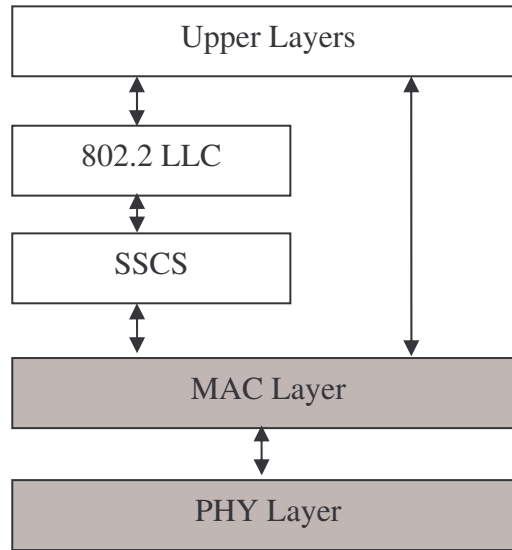


Figure 3. IEEE 802.15.4 LR-WPAN device architecture (from [8]).

The IEEE 802.15.4 standard defines the physical layer (PHY) and the medium access layer (MAC). An IEEE 802.2 Type 1 logical link control (LLC) can access the MAC layer through the service specific convergence sub-layer (SSCS). The PHY layer specifies an operating frequency of 2.4 GHz with a basic bit rate of 250 kbps. There are alternate PHY specifications for 915 MHz and 868 MHz that operate at lower data rates of 40 kbps and 20 kbps, respectively. Details of the LR-WPAN modulation and spreading formats are summarized in Table 1.

PHY(MHz)	Frequency band (MHz)	Spreading parameters		Data parameters		
		Chip rate (kchips/s)	Modulation	Bit rate (kb/s)	Symbol rate (ksym/s)	Symbols
868	868-868.6	300	BPSK	20	20	Binary
915	902-928	600	BPSK	40	40	Binary
2450	2400-2483.5	2000	O-QPSK	250	62.5	16-ary Orthogonal

Table 1. IEEE 802.15.4 LR-WPAN frequency bands and data rates (from [8]).

### ***b. LR-WPAN Network Topologies***

Depending on the application requirements, the LR-WPAN may operate in one of the two topologies shown in Figure 4: Star Topology or Peer-to-Peer Topology. In the Star Topology, the communication is established between devices and a single central controller, called the Personal Area Network (PAN) coordinator. Peer-to-Peer Topology also has a PAN coordinator; however, it differs from the star topology in that any device can communicate with any other device as long as they are within range of one another.

Peer-to-Peer Topology allows more complex network formations to be implemented, such as mesh networking. A peer-to-peer network can be ad hoc, self-organizing and self-healing. It may also allow multiple hops to route messages from any device to any other device on the network.

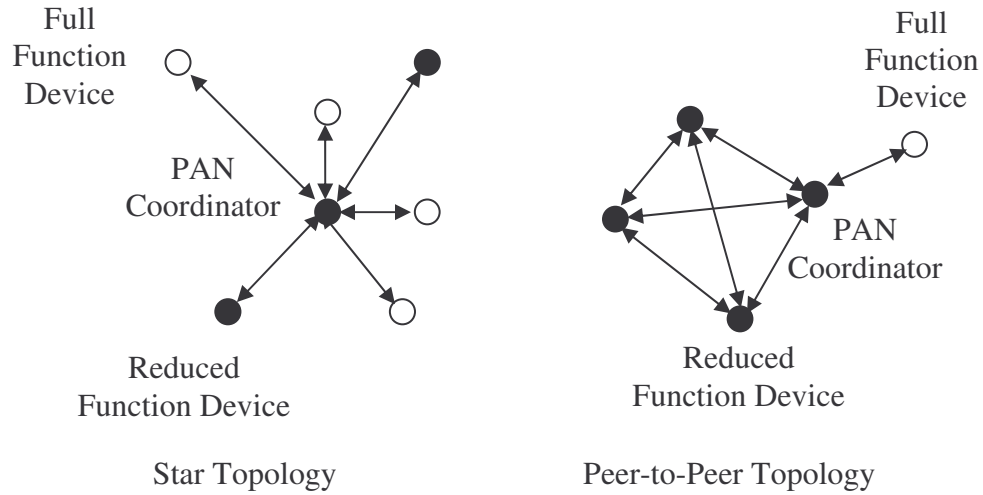


Figure 4. Star and Peer-to-Peer topologies for a IEEE 802.15.4 LR-WPAN (from [8]).

To form a larger network, supporting hundreds and thousands of sensor nodes, a single sensor cluster can reorganize and form a mesh of multiple neighboring clusters. Once predetermined application or network requirements are met, the PAN coordinator may instruct a device to become the cluster head of a new cluster adjacent to the first one. Other devices gradually connect and form a multi-cluster network structure, such as the one seen in Figure 5. The advantage of a multi-cluster structure is increased coverage area; the disadvantage is an increase in message latency.

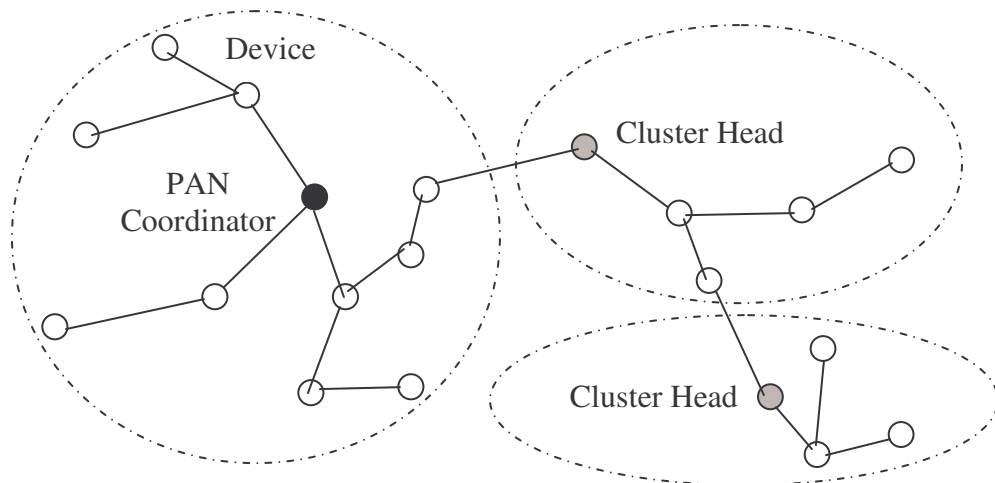


Figure 5. IEEE 802.15.4 LR-WPAN cluster tree network (from [8]).



## B. ACOUSTIC SOURCE LOCALIZATION

Sound localization can be accomplished by using observed differences in the sound signals received at different observation points, such as angle of arrival (AOA), time of arrival (TOA), time difference of arrival (TDOA), received signal strength (RSS) or steered response power (SRP), to estimate the direction and actual location of the sound source. Several methods, usually based on SRP and TDOA, have been developed for estimating an acoustical source location.

Algorithms, like Steered Response Power-Phase Transform (SRP-PHAT) [10], are robust in the presence of reverberation. However, SRP-PHAT can be quite complex requiring the calculation of a large number of test points in the region of possible source locations. The location is chosen to be the point that produces the highest steered response power.

Alternatively, the problem can be implemented as a two-step localization process [11]. In a two-step localization approach, the time difference of arrival (TDOA) is first determined by performing cross-correlation on the received signals [12]. The TDOA values are then used to estimate the location.

There are generally three classes of TDOA estimators [12], including the general cross-correlation (GCC) approach, the maximum likelihood (ML) approach, and the phase transform (PHAT) approach. All these approaches attempt to calculate the cross-correlation in an optimal or suboptimal manner, and then select the time index of the peak of the result to be the TDOA estimate.

The two-step localization algorithms are quite fast, but they lack robustness [12]. Frequently, errors do occur in the time delay estimates due to reflections of the sound source, which are sometimes greater in energy than the direct signal. The direct path can be obstructed or attenuated because of source and microphone directivity. Erroneous time delay estimates cause large errors in location estimation.

For the counter-sniper application studied in this thesis, we propose the use of the two-step localization process due to its speed and the limited computational capabilities of the sensors.

### C. SNIPER DETECTION

A gun shot produces several detectable phenomena, such as muzzle blast and shockwaves [3] [6].

Muzzle blast is the acoustic signature associated with the ejection of the bullet from the sniper's rifle. The muzzle blast is a loud, characteristic noise originating from the end of the muzzle and propagating spherically away at the speed of sound. The muzzle blast can be detected with acoustic sensors at ranges from several hundred meters out to more than a kilometer.

Typical rifles fire projectiles at supersonic velocities, thereby producing acoustic shocks along their trajectory. Shockwaves can be detected acoustically at ranges from hundreds of meters out to more than a kilometer and can be used to accurately determine projectile trajectories. The shock waveform is distinctive and cannot be produced by any other natural phenomenon.

As illustrated in Figure 6, the muzzle blast and shockwaves can be detected and processed by distributed wireless sensor networks equipped with acoustic sensors.

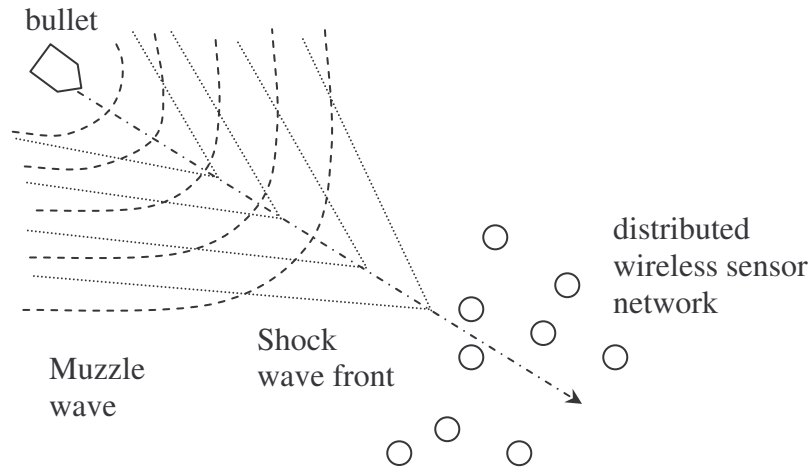


Figure 6. Shock wave front and muzzle wave detection by a group of distributed wireless sensors (after [4]).

As illustrated in Figure 7, wireless sensors may be mounted on vehicles for easy and fast deployment. The wireless sensors can also be worn on soldiers or integrated into their helmets.

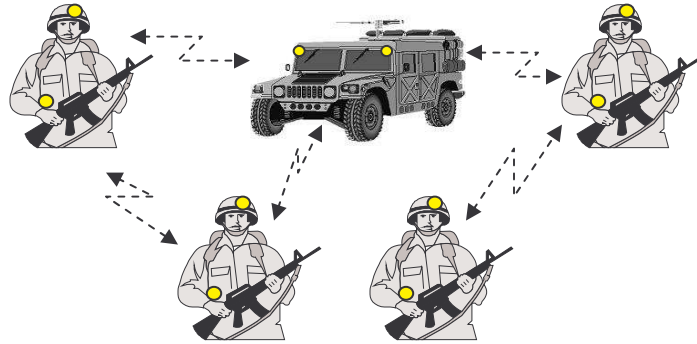


Figure 7. Wireless network-based counter-sniper system consisting of vehicular and wearable sensors.

We have introduced the basics of wireless sensor networks, described the concept of source localization for acoustic signal sources and proposed the concept of using wireless sensor networks to detect sniper fire. In the next chapter, we will discuss in greater detail the various source localization techniques. We will discuss the two-step source localization technique proposed for counter-sniper applications.

### III. SOURCE LOCALIZATION USING WIRELESS SENSOR NETWORKS

This chapter presents the details of source localization using distributed sensor networks. We will discuss the two-step source localization technique proposed for counter-sniper applications.

Source localization is the process of determining the spatial location of a source based on multiple observations of the emitted signal source. The primary goal of source localization is accuracy. The accuracy of location estimates depends on a number of factors, including quantity and quality of sensors used, sensor placement relative to each other and the signal sources to be analyzed, ambient noise and reverberation, and number of active sources and their spectral content. The performance of localization techniques generally improves with the number of sensors in the array, especially when adverse environmental conditions are present.

#### A. TWO-STEP LOCALIZATION PROCESS

Figure 8 shows the schematic diagram of the two-step source localization technique considered in this thesis. The generalized cross correlation (GCC) technique is used to estimate the time difference of arrival  $\hat{\tau}_{12}$  for a pair of received signals  $m_1(t)$  and  $m_2(t)$ .

The  $\hat{\tau}_{12}$  values are then converted into range difference of arrival  $\hat{d}_{12}$  values using the relationship

$$\hat{d}_{12} = \hat{\tau}_{12}v$$

where  $v = 345$  m/s is the speed of sound [12]. Figure 9 shows the range difference of arrival at two acoustic sensors. The  $\hat{d}_{12}$  values along with the knowledge of the sensor positions are then used to generate hyperbolic curves which are then intersected to obtain a source location estimate.

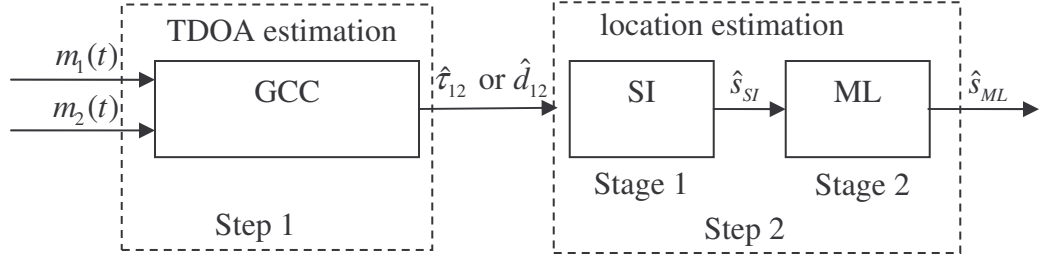


Figure 8. Two-step source localization model using GCC and hybrid SI/ML methods. Step 1 performs the TDOA estimation using GCC; Step 2 performs the location estimation in two stages: estimate determined by SI method in stage 1 is used as initial values for ML method in stage 2.

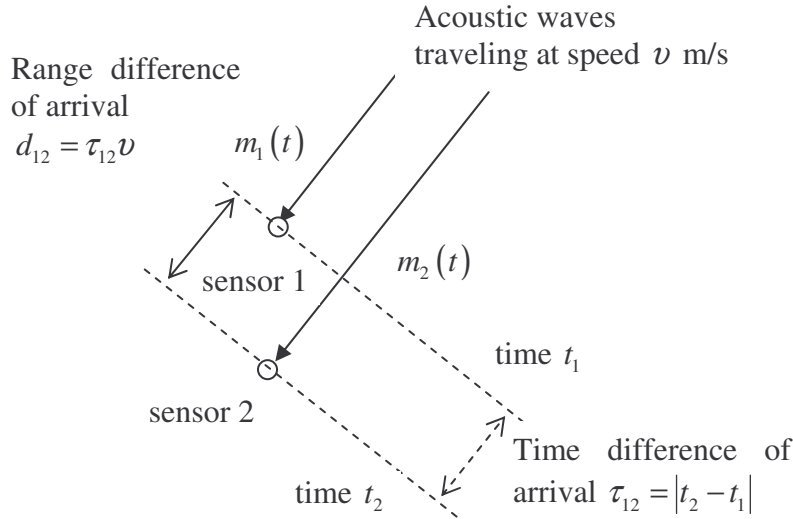


Figure 9. Range difference of arrival at two acoustic sensors.

Location estimation can be performed using either a closed-form least-squares (LS) [13] or a maximum likelihood (ML) method [14]. The LS method is fast, and a closed-form solution can be obtained in a single iteration. The spherical interpolation (SI) method [13] is a widely used LS implementation in location estimation problems. In contrast, the ML method requires iterative gradient-descent search, and a good initial guess close to the solution is required in order to avoid divergence. However, the ML estimator is asymptotically unbiased and provides a more accurate estimate at low noise levels.

In this work, we propose the use of a hybrid SI/ML algorithm [14] for location estimation using the two-stage process, as illustrated in Figure 8: First, we calculate the source location  $\hat{s}_{SI}$  using spherical interpolation (SI) method. The estimate of the source location  $\hat{s}_{SI}$  is then used as initial value for the calculation of source location  $\hat{s}_{ML}$  using the maximum likelihood (ML) method. A hybrid SI/ML algorithm has been proposed by Ajdler et al. [14] to perform acoustic source localization in a small room of size 3 m  $\times$  5 m  $\times$  3 m. In this thesis, a similar hybrid SI/ML algorithm is applied for acoustic source localization in an outdoor environment instead to detect sniper fire.

At low noise levels, the SI method provides a rough estimate quickly. The ML method is computationally demanding and requires the use of an iterative technique, such as Gauss-Newton and Levenberg-Marquardt [15]. The convergence speed of the ML method can be increased by using the rough estimate from the SI method as initial estimate. Additionally, in situations where the ML method fails to converge, especially at high noise levels, the SI method can still provide a reasonable estimate.

Other closed-form estimation methods like spherical intersection (SX) [13], planar intersection (PX) [13], and clustering-based techniques [16] can also be used to produce the initial guess of the source location. However, the SI method has greater noise immunity than the SX method and the SI method has lower error variance but slightly higher bias than the PX method. Clustering-based techniques are computationally less demanding than the SI method but are only applicable to sources that are very far away.

Alternatively, the ML optimization problem can be solved by using alternating projection method [17] to avoid exhaustive multi-dimensional search. However, this is computationally more intensive than the closed-form methods and there is still no guarantee that the convergence to a global minimum can be obtained.

## 1. Time Difference of Arrival Estimation

Let  $m_1(t)$  and  $m_2(t)$  represent the time-delayed signals of a source signal received at two sensors as shown in Figure 9. If  $M_1(\omega)$  and  $M_2(\omega)$  represent the Fourier transforms of received signals  $m_1(t)$  and  $m_2(t)$ , respectively, the TDOA  $\hat{\tau}$  can be estimated using the GCC given as [12]

$$\hat{\tau} = \arg \max_{\beta} \int_{-\infty}^{\infty} W(\omega) M_1(\omega) M_2^*(\omega) e^{j\omega\beta} d\omega$$

where  $\hat{\tau}$  is an estimate of the delay between original source signal and the two sensors, and  $W(\omega)$  is the GCC weighting function.

Common GCC weighting functions include maximum likelihood (ML) and phase transform (PHAT) [12]:

$$W_{ML}(\omega) = \frac{|M_1(\omega)| |M_2(\omega)|}{|N_1(\omega)|^2 |M_2(\omega)|^2 + |N_2(\omega)|^2 |M_1(\omega)|^2}$$

$$W_{PHAT}(\omega) = \frac{1}{|M_1(\omega) M_2^*(\omega)|}$$

where  $N_1(\omega)$  and  $N_2(\omega)$  are the estimated noise spectral density for the first and second sensors, respectively.

Phase transform (PHAT) uses only the phase information derived from their respective signal power spectral density [12]. This phase-only procedure has the whitening effect on the signals and emphasizes primarily the channel effect. The PHAT has a peak at the relative time delay of the two signals and is used to estimate the TDOA information.

The ML weights require knowledge about the spectrum of the sensor-dependent noises. The PHAT weights do not require this knowledge, and hence has been employed more often due to its simplicity. We choose the GCC-PHAT method due to its ability to reduce the degradation due to reverberation [10].

## 2. Least-squares Spherical Interpolation (SI) Method

The Spherical Interpolation method [13] is chosen for the closed-form least-squares (LS) source location estimation based on the measured range difference of arrival (RDOA) values. Figure 10 shows the notations used in SI method for a single source and two sensors  $i$  and the reference sensor 1.

Let  $N$  denote the number of sensors. The vector of the spatial coordinates for the  $i$ -th sensor is denoted by  $\underline{x}_i = [x_i \ y_i \ z_i]^T$  and the estimated position of the source is denoted by  $\underline{\hat{s}} = [x_s \ y_s \ z_s]^T$ . Sensor 1 is arbitrary selected as the reference node and thus the position of sensor 1 is set as the origin of the coordinate system (i.e.,  $\underline{x}_1 = \underline{0}$ ). The distance between the source and sensor  $i$  is denoted by the Euclidean norm

$$D_i = \|\underline{x}_i - \underline{\hat{s}}\| = \sqrt{(x_i - x_s)^2 + (y_i - y_s)^2 + (z_i - z_s)^2}$$

and the distance from the origin to the point  $\underline{x}_i$  is denoted by  $R_i = \|\underline{x}_i\|$ . Similarly, the estimated distance from the origin to the source is denoted by  $\hat{R}_s = \|\underline{\hat{s}}\|$ . The measured RDOA between sensor  $i$  and sensor 1 is denoted by

$$\hat{d}_{i1} = D_i - D_1 = D_i - \hat{R}_s$$

for  $i = 2, \dots, N$ .



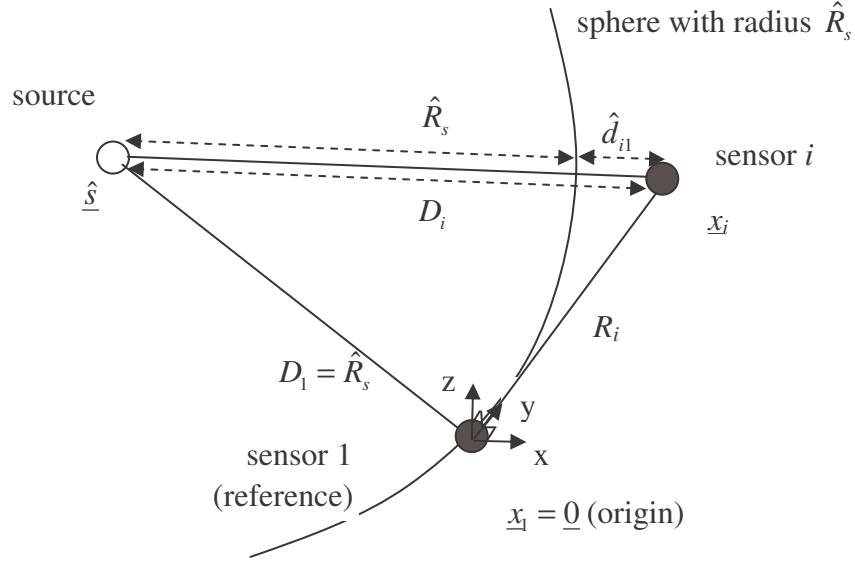


Figure 10. Notations used in Spherical Interpolation (SI) method for a single source, sensor  $i$  and the reference sensor 1 (from [13]).

Assuming that sensor 1 is selected as the reference node (i.e.,  $\underline{x}_1 = \underline{0}$ ), it can be shown [13] that the source location estimate is given as

$$\underline{\hat{s}} = \frac{1}{2} \left( S^T P_d^\perp W P_d^\perp S \right)^{-1} S^T P_d^{\perp T} W P_d^\perp \underline{\delta}.$$

where the projection matrix  $P_d^\perp = I - \frac{d d^T}{d^T d}$ ,

$$\underline{\delta} = \begin{bmatrix} R_2^2 - d_{21}^2 \\ R_3^2 - d_{31}^2 \\ \vdots \\ R_N^2 - d_{N1}^2 \end{bmatrix},$$

the range difference of arrival vector,  $\underline{d} = \begin{bmatrix} d_{21} \\ d_{31} \\ \vdots \\ d_{N1} \end{bmatrix}$ ,

the sensor location matrix,  $S = \begin{bmatrix} x_2 & y_2 & z_2 \\ x_3 & y_3 & z_3 \\ \vdots & \vdots & \vdots \\ x_N & y_N & z_N \end{bmatrix}$ ,

and the weight matrix,  $W = \begin{bmatrix} w_{11} & w_{12} & \cdots & w_{1N} \\ w_{21} & w_{22} & \cdots & w_{2N} \\ \vdots & \vdots & \vdots & \vdots \\ w_{N1} & w_{N2} & \cdots & w_{NN} \end{bmatrix}$ .

The range estimate is given as the Euclidean norm from the origin at sensor 1 to the source

$$\hat{R}_s = \|\underline{\hat{s}}\| = \sqrt{x_s^2 + y_s^2 + z_s^2}$$

and the bearing estimate  $\cos \hat{\Omega}_s$  is defined as the direction cosines from the origin at sensor 1 to the source

$$\cos \hat{\Omega}_s = \frac{\hat{s}}{\hat{R}_s} = \frac{\underline{\hat{s}}}{\|\underline{\hat{s}}\|}.$$

The bearing estimate  $\cos \hat{\Omega}_s$  is equivalent to the unit vector of the source location estimate  $\underline{\hat{s}}$ , as shown in Figure 11.

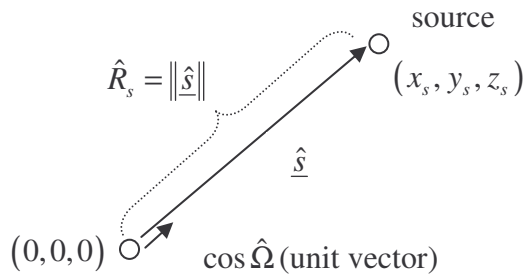


Figure 11. Range and bearing estimate of source location.

### 3. Maximum Likelihood Estimator

The errors  $\eta$  in the measurement of the range difference of arrival (RDOA)  $d_{ij}$  are assumed to be zero mean Gaussian and independent for each sensor. We define  $\Sigma$  as the covariance matrix of the noise vector,  $\Delta$  as the vector of all the exactly measured RDOAs, and  $\Gamma$  as the vector containing the noisy measurements:

$$\Gamma = \Delta + \eta.$$

Assuming that sensor 1 is chosen as the reference node, it can be shown [14] that the likelihood function of  $\Gamma$  given the source location  $\underline{s}$  is

$$f(\Gamma, \underline{s}) = \frac{1}{2\pi^{\frac{(N-1)}{2}} |\Sigma|^{\frac{1}{2}}} e^{-\frac{1}{2} h^T(\underline{s}) \Sigma^{-1} h(\underline{s})} \quad (1.1)$$

where the RDOA error vector  $h(\underline{s})$  is represented by

$$h(\underline{s}) = \begin{bmatrix} \|\underline{s} - \underline{x}_2\| - \|\underline{s} - \underline{x}_1\| - \hat{d}_{12} \\ \|\underline{s} - \underline{x}_3\| - \|\underline{s} - \underline{x}_1\| - \hat{d}_{13} \\ \vdots \\ \|\underline{s} - \underline{x}_N\| - \|\underline{s} - \underline{x}_1\| - \hat{d}_{1N} \end{bmatrix}, \quad (1.2)$$

the noise covariance matrix is represented by

$$\Sigma = \sigma_N^2 \begin{bmatrix} 1 & \frac{1}{2} & \cdots & \frac{1}{2} \\ \frac{1}{2} & 1 & \cdots & \frac{1}{2} \\ \vdots & \vdots & \ddots & \vdots \\ \frac{1}{2} & \frac{1}{2} & \cdots & 1 \end{bmatrix}, \quad (1.3)$$

and the ML cost function is the exponent

$$J_{ML}(\underline{s}) = h^T(\underline{s}) \Sigma^{-1} h(\underline{s}). \quad (1.4)$$

From Equation (1.1) and Equation (1.4), it can be seen that maximizing the likelihood function  $f(\Gamma, \underline{s})$  is equivalent to minimizing the ML cost function  $J_{ML}(\underline{s})$ .

Hence, the source location estimate  $\hat{\underline{s}}_{ML}$  is obtained by minimizing the ML cost function

$$\hat{\underline{s}}_{ML} = \arg \min_{\underline{s}} J_{ML}(\underline{s}).$$

The cost function  $J_{ML}(\underline{s})$  can be minimized using standard numerical optimization methods. The Levenberg-Marquardt method [15] provided by MATLAB is used to solve the minimization problem.

#### 4. Cramer Rao Lower Bound

The minimum mean-squared error for any estimate of a non-random parameter is given by the Cramer Rao Bound [18]. The Cramer Rao Bound (CRB) gives a lower bound on the error variance of any unbiased estimate. The variance of any unbiased estimator of  $\underline{s}$  is bounded by

$$E\left[(\hat{\underline{s}} - \underline{s})(\hat{\underline{s}} - \underline{s})^T\right] \geq F^{-1}(\underline{s}) \quad (1.5)$$

where  $F(\underline{s})$  is the Fischer information matrix, expressed as

$$F(\underline{s}) = E\left\{\left[\frac{\partial \log f(\Gamma, \underline{s})}{\partial \underline{s}}\right]\left[\frac{\partial \log f(\Gamma, \underline{s})}{\partial \underline{s}}\right]^T\right\} \quad (1.6)$$

where  $\Gamma$  is the vector containing the noisy RDOA measurements and  $f(\Gamma, \underline{s})$  is the likelihood function of  $\Gamma$  given the source location  $\underline{s}$ .

From Equation (1.1) and Equation (1.6), it can be shown that [14]

$$F(\underline{s}) = \left[\frac{\partial h(\underline{s})}{\partial \underline{s}}\right]^T \Sigma^{-1} \left[\frac{\partial h(\underline{s})}{\partial \underline{s}}\right] = \mathbf{J}(\underline{s})^T \Sigma^{-1} \mathbf{J}(\underline{s}) \quad (1.7)$$

where  $\mathbf{J}(\underline{s})$  is the Jacobian matrix

$$\mathbf{J}(\underline{s}) = \begin{bmatrix} \frac{(\underline{s} - \underline{x}_2)^T}{\|\underline{s} - \underline{x}_2\|} - \frac{(\underline{s} - \underline{x}_1)^T}{\|\underline{s} - \underline{x}_1\|} \\ \vdots \\ \frac{(\underline{s} - \underline{x}_N)^T}{\|\underline{s} - \underline{x}_N\|} - \frac{(\underline{s} - \underline{x}_1)^T}{\|\underline{s} - \underline{x}_1\|} \end{bmatrix}.$$

From Equation (1.5) and Equation (1.7), it can be shown that the minimum variance of the estimates of the source position is equal to the trace of the inverse of the Fischer information matrix [14]

$$\min E \left[ (\hat{\underline{s}} - \underline{s})(\hat{\underline{s}} - \underline{s})^T \right] = \text{tr} \left( F^{-1}(\underline{s}) \right). \quad (1.8)$$

Each diagonal element of the inverse Fischer information matrix corresponds to the minimal variance of one coordinate of the source position. The total variance on the estimation of the source position is the trace of the inverse Fischer information matrix. It can be shown [14] that the bound on the variance of the source location estimate is directly proportional to the noise variance.

This chapter discussed the two-step source localization technique proposed for our counter-sniper applications. The generalized cross correlation scheme used to determine the time difference of arrival was briefly discussed and the least-squares spherical interpolation (SI) and maximum likelihood (ML) techniques have been summarized. In the next chapter, we will present the simulation results of the hybrid SI/ML estimation method as well as study the network throughput, delay and jitters of the wireless networks.

## IV. SIMULATION RESULTS AND ANALYSIS

In this study, the two-step source localization process, as discussed in Chapter III, is used to estimate the sniper location through the use of wireless sensor nodes forming a distributed sensor network to detect sniper fire. The generalized cross correlation (GCC) technique, as shown in Figure 8, is first used to estimate the time difference of arrival (TDOA) of the received acoustic signals at the sensors. The TDOA values, as shown in Figure 9, are then converted into range difference of arrival (RDOA) values to be used in the hybrid SI/ML estimation method to estimate the source location.

This chapter presents the simulation model of the two-step source localization process, followed by the simulation results of the hybrid SI/ML estimation method using the MATLAB package simulating a sniper detection scenario. The MATLAB code used for the simulation is provided in Appendix. The throughput, delay and jitter of the wireless sensor network are simulated using the NS-2 network simulator.

### A. SIMULATION MODEL

A simulation model is developed in MATLAB to study the two-step localization process. Figure 12 shows the simulation block diagram for the study of the two-step localization process. The study of the TDOA estimation using the GCC technique is carried out by examining the received signals at the sensors. The study of the hybrid SI/ML estimation is carried out separately by representing TDOA values as RDOA and modeling RDOA estimation errors as Gaussian noise [14]. The acoustic source is not explicitly simulated in this work.

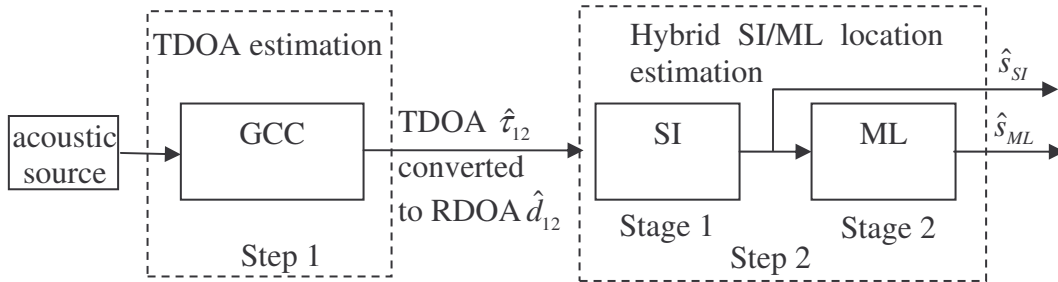


Figure 12. Simulation block diagram for the study of the two-step localization process (based on Figure 8 in Chapter III).

## 1. Time Difference of Arrival Estimation

In the simulation model, based on the known positions of the source and sensors, time-delayed copies of a source signal are generated for each sensor. We now consider the scenario of two sensors (see Figure 9). Figure 13 shows the simulated received signals at sensors 1 and 2. The received signal at sensor 2 is the same as the signal received at sensor 1 but is time delayed by  $\tau_{12} = 40$  ms.

The TDOA between the two sensors is determined using the GCC method as has been discussed in Chapter III. By applying the GCC technique on the two received signals, the TDOA estimate  $\hat{\tau}_{12}$  is determined to be 40.6 ms, which is close to the actual value of  $\tau_{12} = 40$  ms.

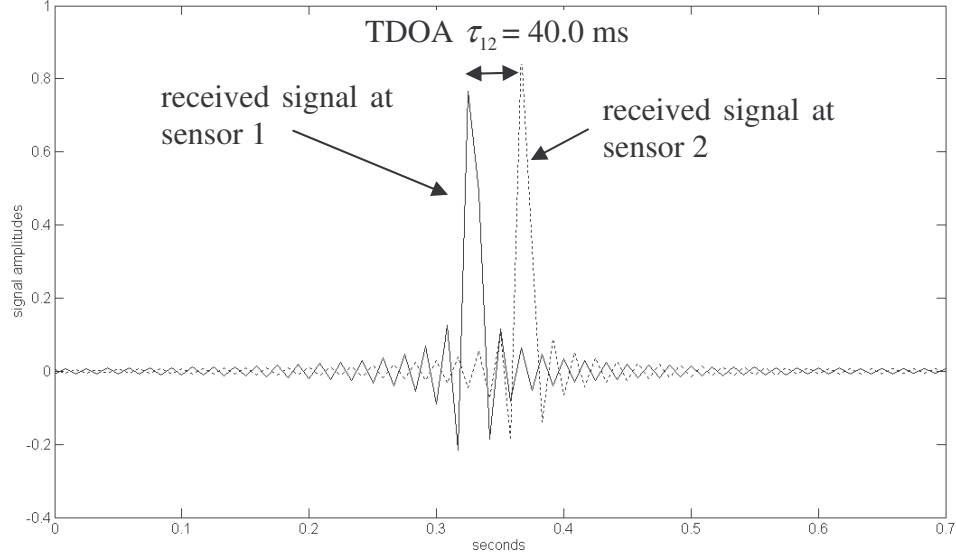


Figure 13. Received signals at two sensors. The received signal at sensor 2 is same as the signal received at sensor 1 but is time delayed by  $\tau_{12} = 40$  ms.

## 2. Hybrid SI/ML Location Estimation

To study the hybrid SI/ML location estimation method proposed in the two-step localization process for counter-sniper applications, the TDOA information  $\hat{\tau}_{ij}$  determined using the GCC technique is now converted into RDOA values  $\hat{d}_{ij}$  using the relationship  $\hat{d}_{ij} = \hat{\tau}_{ij}v$  where  $v = 345$  m/s is the speed of sound [12]. In the simulation

study, however, the GCC method is not used. Instead, we have chosen to generate the measured RDOA values using an additive white Gaussian model as described below.

The true RDOA  $d_{ij}$  values can be determined using the known source and sensor positions that are defined in the simulation scenario. Figure 14 shows the range difference of arrival for a single source and two sensors; sensor 1 is chosen to be the reference sensor. The locations of the source, sensor 2, and sensor 1 are  $(x_s, y_s, z_s)$ ,  $(x_2, y_2, z_2)$  and  $(0,0,0)$ , respectively. The distances  $D_1$  and  $D_2$  are the Euclidean norms between the source and sensor 1 and the source and sensor 2, respectively. The RDOA  $d_{12}$  between sensor 1 and sensor 2 is given by

$$d_{12} = D_1 - D_2 = \tau_{12}v$$

where  $\tau_{12} = |t_1 - t_2|$  is the magnitude of the difference between the time of arrival  $t_1$  at sensor 1 and the time of arrival  $t_2$  at sensor 2.

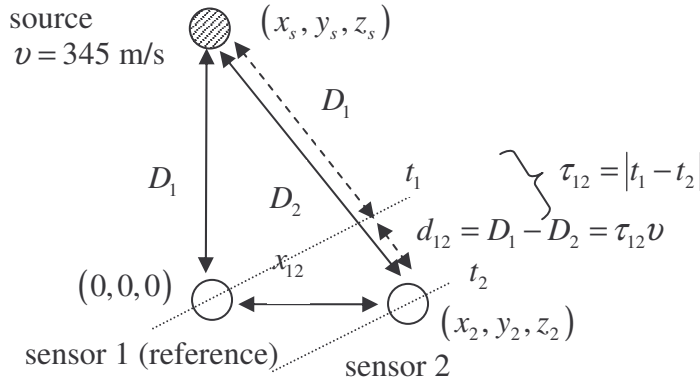


Figure 14. Range difference of arrival  $d_{12}$  for a single source, sensor 2 and reference sensor 1 located at  $(x_s, y_s, z_s)$ ,  $(x_2, y_2, z_2)$  and  $(0,0,0)$ , respectively.

The measured RDOA values  $\hat{d}_{ij}$  are modeled as

$$\hat{d}_{ij} = d_{ij} + n$$

where  $n$  is a white Gaussian noise with zero mean and variance  $\sigma_n^2$ . Figure 15 illustrates the additive white Gaussian noise model used to generate the measured RDOA values



$\hat{d}_{ij}$ . The true RDOA values  $d_{ij}$  are determined using the known sensor and source positions as illustrated in Figure 14.

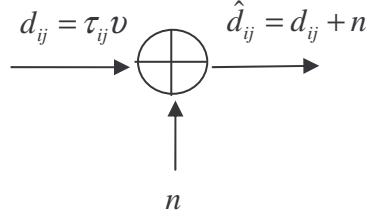


Figure 15. Modeling of range difference of arrival (RDOA).

The  $\hat{d}_{ij}$  values are then used in the hybrid SI/ML estimation method to estimate the source location. As discussed in Chapter III, the hybrid SI/ML estimation method consists of two stages. As shown in Figure 12, the first stage of the hybrid SI/ML method produces the location estimate using the SI method. The SI estimate is then used to provide initial values for the iterative ML method used in the second stage. In the simulation study, location estimation performance of both SI and ML are studied using the performance metrics described below.

Monte Carlo simulation runs are carried out and the estimated source location coordinates  $\hat{s}_i$  are compared with the actual source location coordinates  $s$  to obtain the performance metrics of error mean

$$\mu = \frac{1}{M} \sum_{i=1}^M (\hat{s}_i - s)$$

error variance

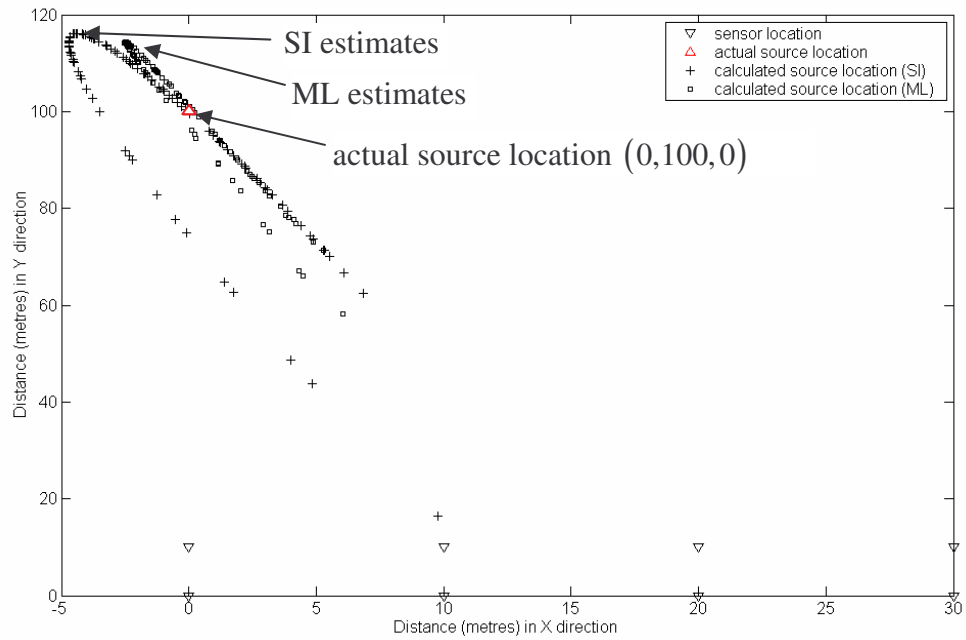
$$\sigma^2 = \frac{1}{M} \sum_{i=1}^M (\hat{s}_i - s - \mu)^2$$

and root mean square (RMS) error given by square root of the second moment

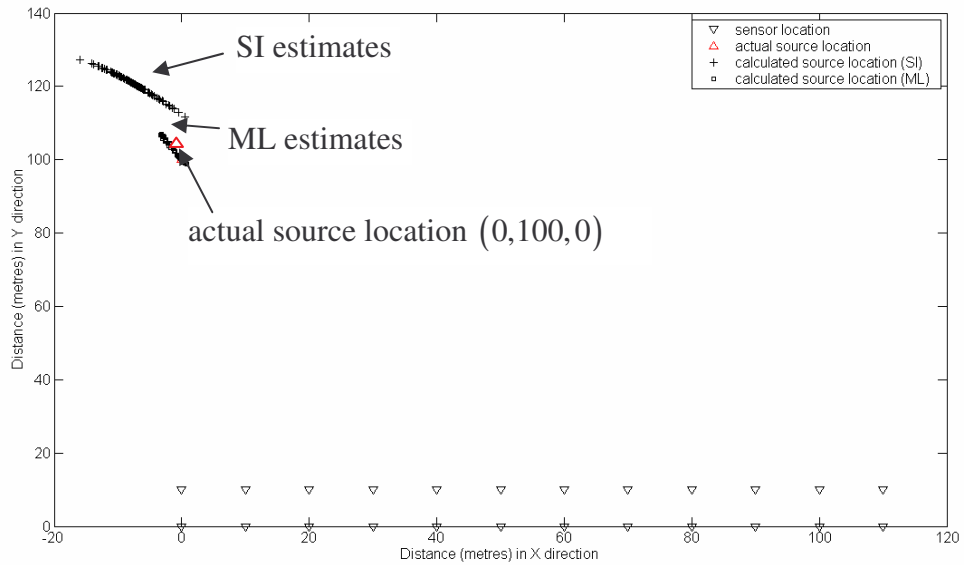
$$\gamma = \sqrt{\mu^2 + \sigma^2}$$

where  $M$  is the number of simulation runs.

Figure 16 shows location estimates of 100 Monte Carlo simulation runs of the SI and ML methods in a scenario with the source at 100 m from the origin; the sensors are spaced 10 m apart. Table 2 shows the error mean  $\mu$ , error variance  $\sigma^2$  and RMS error  $\gamma$  for 24 and 72 sensor nodes for the SI and ML methods. The notations  $Xs\_SI$ ,  $Ys\_SI$ ,  $Zs\_SI$ ,  $Rs\_SI$  and  $Bearing\_SI$  refer to the individual  $X$ ,  $Y$ ,  $Z$  range and bearing readings, respectively, for the SI method used in the first stage of the hybrid SI/ML method. Similarly, the notations  $Xs\_ML$ ,  $Ys\_ML$ ,  $Zs\_ML$ ,  $Rs\_ML$  and  $Bearing\_ML$  refer to the individual  $X$ ,  $Y$ ,  $Z$  range and bearing readings, respectively, for the ML method used in the second stage. From Figure 16, the estimated locations do not coincide with the actual source location at (0,100,0). For the case of 24 sensor nodes, the error variance  $\sigma^2$  is large and the position estimates are widely scattered. For the case of 72 sensor nodes, however, the ML method produces estimation with a low RMS error of less than 3 m, and the position estimates are closer to the source at (0,100,0).



(a)



(b)

Figure 16. Simulation output of the location estimation using the SI and ML methods in a scenario with the source at 100 m from the origin and the sensors spaced 10 m apart: (a) 24 sensor nodes and (b) 72 sensor nodes. The number of Monte Carlo runs is 100.

Performance Metrics		Number of Nodes	
		24	72
Error Mean $\mu_{SI}$ in meters	$X_{s\_SI}$	-1.021	-7.6879
	$Y_{s\_SI}$	-2.0383	20.688
	$Z_{s\_SI}$	-1.3407	-0.7423
	$R_{s\_SI}$	-1.8955	20.992
	$Bearing\_SI$	2.8112	3.7754
Error mean $\mu_{ML}$ in meters	$X_{s\_ML}$	0.007947	-0.76399
	$Y_{s\_ML}$	-0.37713	1.6088
	$Z_{s\_ML}$	-0.01764	-0.17491
	$R_{s\_ML}$	-0.32973	1.6182
	$Bearing\_ML$	1.535	0.54189
Error variance $\sigma_{SI}^2$ in square meters	$X_{s\_SI}$	11.914	11.224
	$Y_{s\_SI}$	359.54	10.753
	$Z_{s\_SI}$	7.5425	4.1336
	$R_{s\_SI}$	353.59	12.112
	$Bearing\_SI$	11.599	1.9837
Error variance $\sigma_{ML}^2$ in square meters	$X_{s\_ML}$	5.4121	1.2701
	$Y_{s\_ML}$	196.71	5.7233
	$Z_{s\_ML}$	2.828	0.11484
	$R_{s\_ML}$	195.4	5.7962
	$Bearing\_ML$	1.4399	0.29564
RMS error $\gamma_{SI}$ in meters	$X_{s\_SI}$	3.5996	8.3862
	$Y_{s\_SI}$	19.071	20.946
	$Z_{s\_SI}$	3.0561	2.1644
	$R_{s\_SI}$	18.899	21.279
	$Bearing\_SI$	4.4161	4.0296
RMS error $\gamma_{ML}$ in meters	$X_{s\_ML}$	2.3264	1.3615
	$Y_{s\_ML}$	14.03	2.883
	$Z_{s\_ML}$	1.6818	0.38136
	$R_{s\_ML}$	13.983	2.9008
	$Bearing\_ML$	1.9484	0.76765

Table 2. Mean  $\mu$ , variance  $\sigma^2$ , and RMS value  $\gamma$  of the position errors for the SI and ML methods in a scenario with the source at 100 m from the origin and the sensors spaced 10 m apart. The number of Monte Carlo runs is 100.

## B. HYBRID SI/ML ESTIMATION METHOD SIMULATION

The effects of the number of sensor nodes, inter-sensor spacing, topology, noise, source-sensor distance, sensor node failure, and location perturbation on the estimation performance of the hybrid implementation of the closed-form least-squares spherical interpolation (SI) method and the iterative maximum likelihood (ML) method are studied. The main objective of this portion of the simulation is to study suitable wearable and vehicular sensor node configurations for the counter-sniper application as well as to determine the required number of sensors and the inter-sensor spacing to accurately estimate a source of sniper fire located a few hundred meters away.

Figure 17 shows the schematic of a sensor node topology using the three-dimensional  $XYZ$  Cartesian coordinate system. By setting different source and sensor positions, different simulation scenarios can be constructed. Note that for the sensor node topology with regular inter-sensor spacing, a simplified notation of  $K \times L \times M$  is used to describe a topology that has  $K, L$  and  $M$  sensor nodes along the  $X, Y$  and  $Z$  plane, respectively.

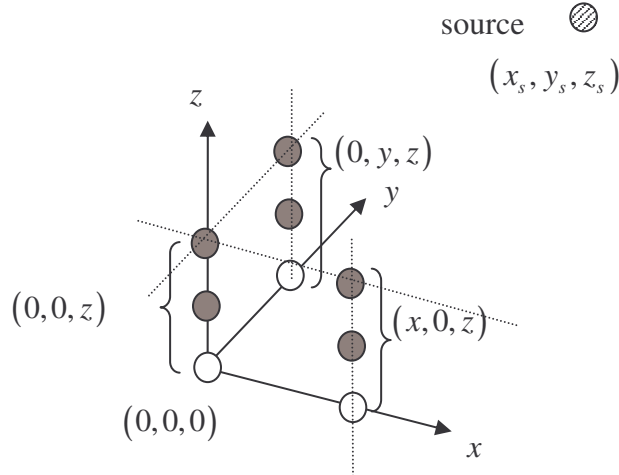


Figure 17. Schematic of the sensor topology using the three-dimensional  $XYZ$  Cartesian coordinate system. White and grey circles represent sensors that are placed in the two-dimensional  $XY$  and the three-dimensional  $XYZ$  planes, respectively.

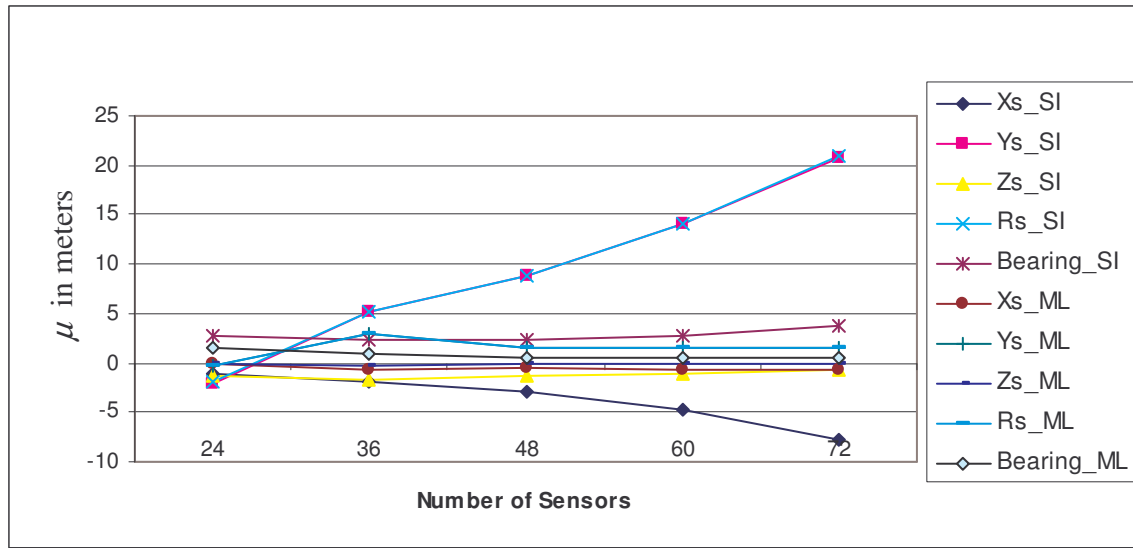
## 1. Effect of Number of Sensor Nodes

The effect of the number of sensor nodes on the location estimation performance is studied using the scenario of a source located 100 m from the origin; the sensors are spaced 10 m apart. Several topologies are formed using 9 (i.e.,  $3 \times 1 \times 3$ ), 12 (i.e.,  $2 \times 2 \times 3$ ), 24 (i.e.,  $4 \times 2 \times 3$ ), 36 (i.e.,  $6 \times 2 \times 3$ ), 48 (i.e.,  $8 \times 2 \times 3$ ), 60 (i.e.,  $10 \times 2 \times 3$ ) and 72 (i.e.,  $12 \times 2 \times 3$ ) sensor nodes. A  $3 \times 1 \times 3$  topology represents a single row of three sensor columns with three sensors each; a  $12 \times 2 \times 3$  topology represents two rows of twelve sensor columns with three sensors each.

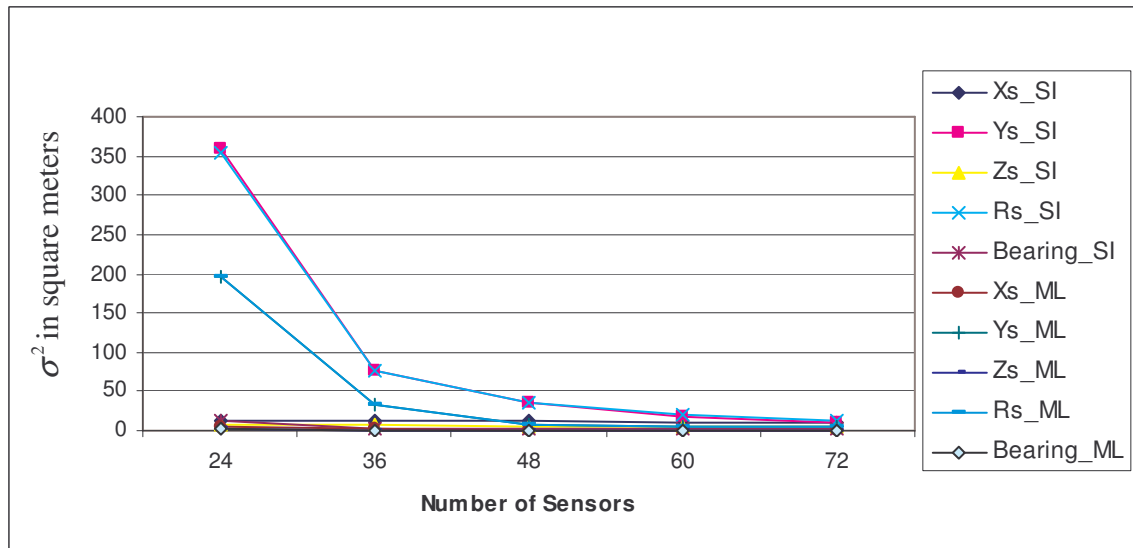
Figure 18 and Table 3 show the error mean  $\mu$ , error variance  $\sigma^2$  and RMS error  $\gamma$  for different sensor node topologies. For the cases of less than 12 sensor nodes, the errors of the ML were very large and are not shown in the plots in Figure 18.

It can be seen that as the number of sensor nodes is increased, the error variance  $\sigma^2$  decreases for both SI and ML methods used in the two stages of the hybrid SI/ML algorithm. For example, when the number of sensors increases from 24 to 48, the error variance  $\sigma^2$  for the  $R_s$  values in the SI stage decreases quickly from  $354 \text{ m}^2$  to  $36 \text{ m}^2$  (approximately). The error variance  $\sigma^2$  of the ML stage is lower than the first SI stage and decreases from  $195 \text{ m}^2$  to  $7 \text{ m}^2$  (approximately). It is observed that when the error variance  $\sigma^2$  of the SI method in the first stage is high (i.e., for the case of 9 and 12 sensor nodes), it led to highly inaccurate results for the ML method in the second stage.

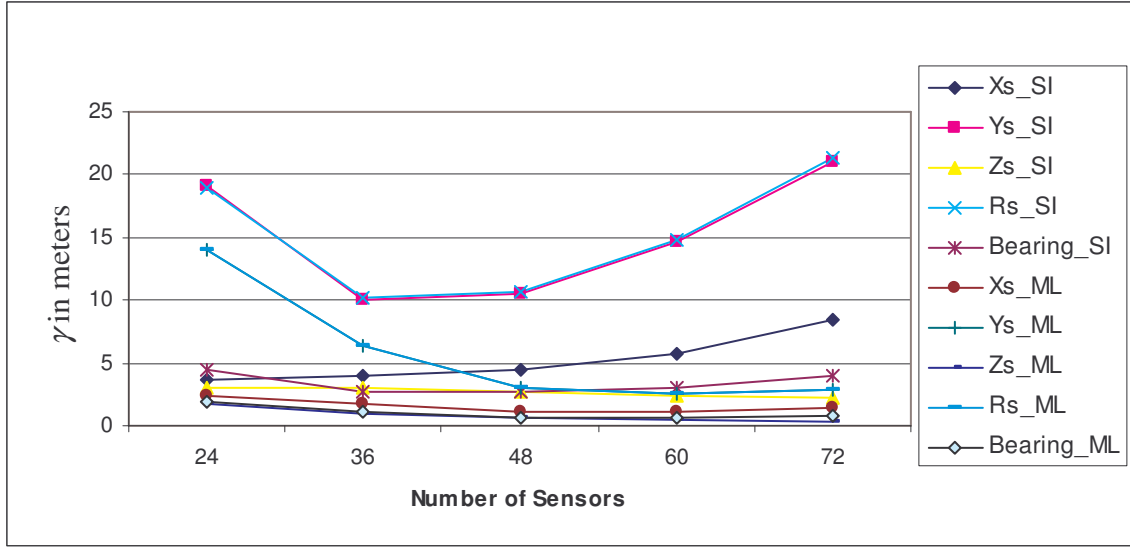
The effect of the bias introduced by the SI method is clearly seen when the number of sensors is very high (i.e., 48 sensors or more). However, the ML method in the second stage is tolerant to the bias introduced by the SI stage. For example, the error mean  $\mu$  for  $R_s$  values using the SI method increased from 9 m to 21 m (approximately) when the number of sensors increased from 48 to 72; however, the RMS error  $\gamma$  for  $R_s$  values for the ML method remained below 3.1 m.



(a)



(b)



(c)

Figure 18. Effect of number of sensor nodes on the location estimation performance of the hybrid SI/ML method: (a) error mean  $\mu$ , (b) error variance  $\sigma^2$ , and (c) RMS error  $\gamma$ . The readings for 9 and 12 sensors are not shown due to highly erroneous results. Results are based on 100 Monte Carlo runs.



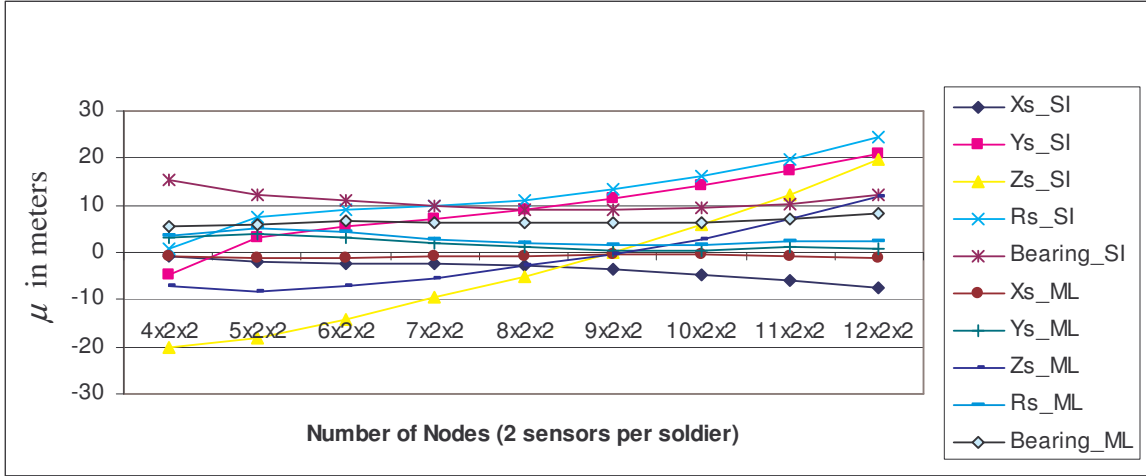
	Number of Nodes	9	12	24	36	48	60	72
Error mean $\mu_{SI}$ in meters	$Xs\_SI$	-0.99945	-0.04349	-1.021	-1.9582	-2.8292	-4.7036	-7.6879
	$Ys\_SI$	-26.868	-30.456	-2.0383	5.0957	8.7197	13.989	20.688
	$Zs\_SI$	1.4638	1.8704	-1.3407	-1.6174	-1.3639	-1.1141	-0.7423
	$Rs\_SI$	-23.144	-26.308	-1.8955	5.2157	8.8395	14.155	20.992
	$Bearing\_SI$	21.487	22.94	2.8112	2.3622	2.2773	2.7098	3.7754
Error mean $\mu_{ML}$ in meters	$Xs\_ML$	-3.49E+08	1.28E+09	0.007947	-0.77733	-0.52786	-0.5967	-0.76399
	$Ys\_ML$	1.60E+08	5.49E+08	-0.37713	2.9459	1.5521	1.4334	1.6088
	$Zs\_ML$	-1.91E+08	7.18E+08	-0.01764	-0.34894	-0.18401	-0.1626	-0.17491
	$Rs\_ML$	4.37E+08	1.57E+09	-0.32973	2.9664	1.5599	1.4398	1.6182
	$Bearing\_ML$	10.497	23.621	1.535	0.97759	0.54588	0.46911	0.54189
Error variance $\sigma_{SI}^2$ in square meters	$Xs\_SI$	10.163	7.3159	11.914	12.586	12.01	11.316	11.224
	$Ys\_SI$	2088.6	2156.9	359.54	75.292	34.693	18.157	10.753
	$Zs\_SI$	22.946	23.819	7.5425	6.8466	5.3038	4.4692	4.1336
	$Rs\_SI$	1560.7	1591.6	353.59	75.748	35.639	19.304	12.112
	$Bearing\_SI$	1970.4	2098.1	11.599	1.8786	1.8306	1.9483	1.9837
Error variance $\sigma_{ML}^2$ in square meters	$Xs\_ML$	1.52E+18	4.12E+16	5.4121	2.6975	1.0198	0.80249	1.2701
	$Ys\_ML$	2.76E+17	7.71E+17	196.71	32.131	6.962	4.2166	5.7233
	$Zs\_ML$	4.79E+17	7.32E+17	2.828	0.90724	0.30799	0.15477	0.11484
	$Rs\_ML$	2.26E+18	1.54E+18	195.4	32.201	6.9973	4.2598	5.7962
	$Bearing\_ML$	447.78	233.55	1.4399	0.34273	0.20057	0.17955	0.29564
RMS error $\gamma_{SI}$ in meters	$Xs\_SI$	3.341	2.7051	3.5996	4.0523	4.4737	5.7827	8.3862
	$Ys\_SI$	53.014	55.538	19.071	10.063	10.523	14.624	20.946
	$Zs\_SI$	5.0089	5.2266	3.0561	3.0761	2.6766	2.3897	2.1644
	$Rs\_SI$	45.786	47.788	18.899	10.146	10.667	14.821	21.279
	$Bearing\_SI$	49.316	51.228	4.4161	2.7311	2.6489	3.0482	4.0296
RMS error $\gamma_{ML}$ in meters	$Xs\_ML$	1.28E+09	2.12E+08	2.3264	1.8171	1.1395	1.0764	1.3615
	$Ys\_ML$	5.49E+08	9.20E+08	14.03	6.3883	3.0612	2.5043	2.883
	$Zs\_ML$	7.18E+08	8.98E+08	1.6818	1.0144	0.58468	0.42569	0.38136
	$Rs\_ML$	1.57E+09	1.30E+09	13.983	6.4032	3.0709	2.5165	2.9008
	$Bearing\_ML$	23.621	17.475	1.9484	1.1395	0.70609	0.63215	0.76765

Table 3. Effect of number of sensor nodes on the location estimation performance of the hybrid SI/ML method: error mean  $\mu$ , error variance  $\sigma^2$ , and RMS error  $\gamma$ . The number of Monte Carlo runs is 100.

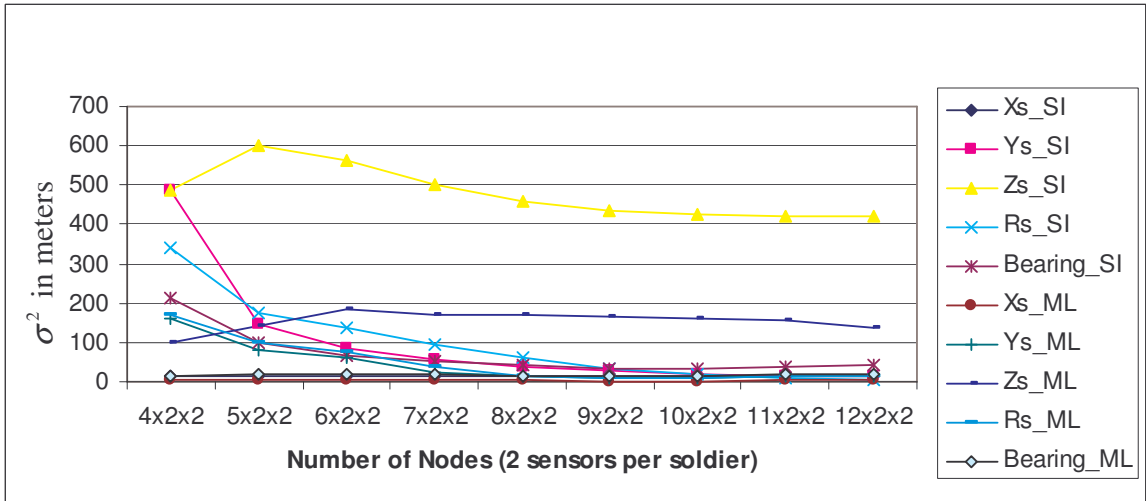
Another scenario is simulated to represent a number of soldiers wearing two sensors spaced 1 m apart. The sensors on the soldier are assumed to be mounted one each on the foot and the helmet. Each soldier is stationed 10 m apart and the source is at 100 m from the origin. This leads to a 3-D sensor node arrangement, and the scenario considered the sensor node arrangements in the range from  $4 \times 2 \times 2$  to  $12 \times 2 \times 2$ . A  $4 \times 2 \times 2$  indicates a total eight soldiers wearing two sensors each in two rows of four soldiers each.

Figure 19 shows the error mean, error variance and RMS error for the different number of soldiers. It can be seen that the estimation accuracy in the  $Z$  direction is poorer than in the  $X$  and  $Y$  directions. For example, for the case of  $5 \times 2 \times 2$ , the RMS errors for the  $X_s$ ,  $Y_s$ , and  $Z_s$  readings at the ML stage are 3 m, 10 m and 14 m, respectively. The poorer accuracy in the  $Z$  direction is due to the constraint that the wearable sensors are only 1 m apart in the  $Z$  direction.

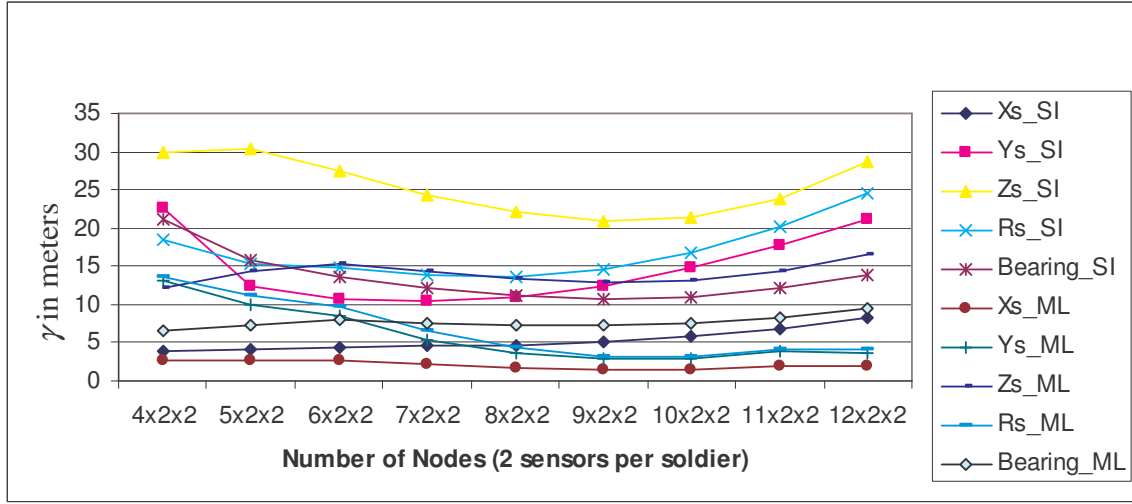
It is observed that by deploying more sensor nodes, the accuracy of the estimation can be improved. For example, twelve soldiers with two sensors each (i.e.,  $6 \times 2 \times 2$ ) can detect a sniper 100 m away with an RMS error  $\gamma$  of 3 m, 8 m and 15 m for the  $X_s$ ,  $Y_s$ , and  $Z_s$  readings, respectively, at the ML stage. However, when the number of soldiers is greater than eighteen, the larger bias introduced by the SI method in the first stage may lead to less accurate estimates for the ML stage, especially for the  $Z_s$  values. For example, forty-eight soldiers ( $12 \times 2 \times 2$ ) can detect a sniper 100 m away with an RMS error  $\gamma$  of 3 m, 4 m and 17 m for the  $X_s$ ,  $Y_s$ , and  $Z_s$  readings, respectively, using the ML method.



(a)



(b)



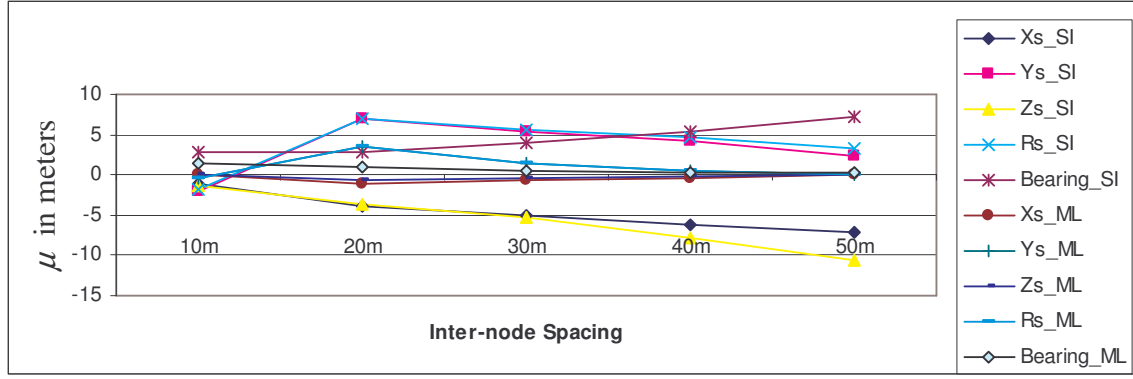
(c)

Figure 19. Performance of the hybrid SI/ML method for simulated wearable configuration (two sensors per soldier) with different number of soldiers: (a) error mean  $\mu$ , (b) error variance  $\sigma^2$ , and (c) RMS error  $\gamma$ . Results are based on 100 Monte Carlo runs.

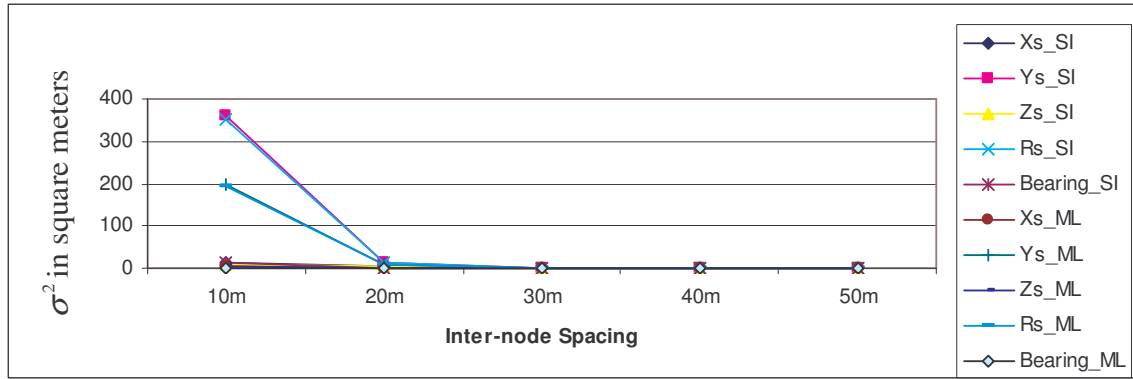
## 2. Effect of Inter-Sensor Spacing

To study the effect of inter-sensor spacing on the location estimation performance, a scenario consisting of 24 sensor nodes ( $6 \times 2 \times 2$ ) is simulated. The source is situated 100 m from the origin and the inter-sensor spacing is varied from 10 m to 50 m. Figure 20 and Table 4 show the error mean  $\mu$ , error variance  $\sigma^2$  and RMS error  $\gamma$  for different inter-sensor spacing.

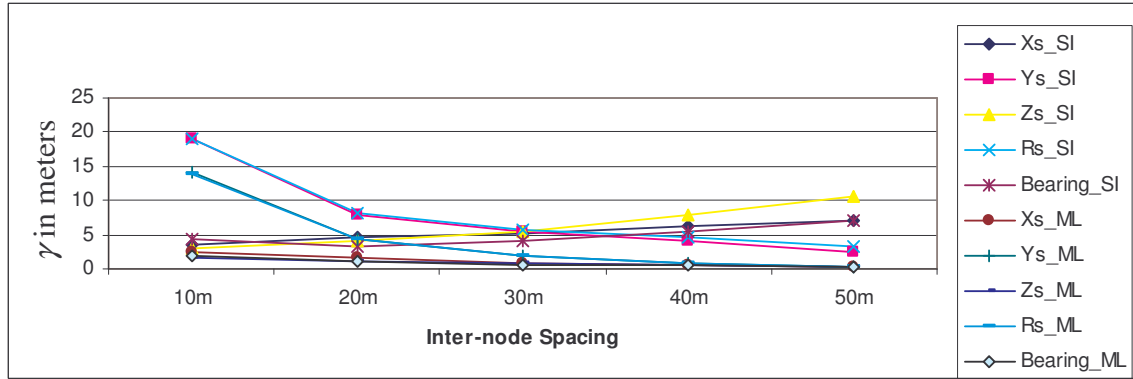
It is observed that when the inter-sensor spacing increases, the estimation accuracy increases. The error variance  $\sigma^2$  decreases rapidly when the inter-sensor spacing is increased. For example, at the inter-sensor spacing of 10 m, the error variance  $\sigma^2$  of the  $R_s$  values obtained at the ML stage was  $195 \text{ m}^2$ ; at the inter-sensor spacing of 20 m, the error variance  $\sigma^2$  quickly decreased to  $7.6 \text{ m}^2$ .



(a)



(b)



(c)

Figure 20. Effect of inter-sensor spacing on location estimation performance of the hybrid SI/ML method : (a) error mean  $\mu$ , (b) error variance  $\sigma^2$ , and (c) RMS error  $\gamma$ . Results are based on 100 Monte Carlo runs.

	Inter-sensor Spacing	1 m	5 m	10 m	20 m	30 m	40 m	50 m
Mean error $\mu_{SI}$ in meters	$X_{S\_SI}$	1.4874	3.8611	-1.021	-3.9662	-5.0268	-6.0904	-7.0891
	$Y_{S\_SI}$	-96.052	-56.341	-2.0383	6.8829	5.3421	4.125	2.4439
	$Z_{S\_SI}$	1.014	2.3276	-1.3407	-3.667	-5.3771	-7.7525	-10.657
	$R_{S\_SI}$	-92.607	-49.787	-1.8955	7.0553	5.6146	4.5986	3.2445
	$Bearing\_SI$	75.399	42.603	2.8112	2.8987	3.9867	5.4073	7.1224
Mean error $\mu_{ML}$ in meters	$X_{S\_ML}$	-6.54E+07	4.01E+07	0.00795	-1.0804	-0.6564	-0.30166	-0.04878
	$Y_{S\_ML}$	1.11E+08	2.03E+08	-0.37713	3.4316	1.5148	0.55075	0.055739
	$Z_{S\_ML}$	-2.82E+07	3.03E+06	-0.01764	-0.75852	-0.50311	-0.24626	-0.04254
	$R_{S\_ML}$	1.35E+08	2.46E+08	-0.32973	3.4495	1.5218	0.55344	0.056847
	$Bearing\_ML$	26.764	10.791	1.535	0.91882	0.57074	0.34763	0.2187
Error variance $\sigma_{SI}^2$ in square meters	$X_{S\_SI}$	0.054935	1.19E+01	11.914	5.0661	2.1157	0.99307	0.451
	$Y_{S\_SI}$	244.13	1.97E+03	359.54	14.286	1.6202	0.1256	0.014497
	$Z_{S\_SI}$	0.024743	5.78E+00	7.5425	3.6117	1.5424	0.7841	0.41151
	$R_{S\_SI}$	208.03	1.38E+03	353.59	15.188	1.9432	0.22131	0.002205
	$Bearing\_SI$	3060.8	3297.6	11.599	1.9415	0.96781	0.4869	0.25618
Error variance $\sigma_{ML}^2$ in square meters	$X_{S\_ML}$	1.64E+16	7.94E+16	5.4121	1.2418	0.44208	0.21931	0.11579
	$Y_{S\_ML}$	4.77E+16	2.39E+17	196.71	7.6353	0.97013	0.20748	0.032234
	$Z_{S\_ML}$	4.07E+15	1.57E+16	2.828	0.81316	0.32197	0.17749	0.10389
	$R_{S\_ML}$	6.74E+16	3.16E+17	195.4	7.7062	0.98182	0.2098	0.032316
	$Bearing\_ML$	709.58	174.95	1.4399	0.27527	0.12701	0.055	0.025056
RMS error $\gamma_{SI}$ in meters	$X_{S\_SI}$	1.64E+16	5.18E+00	3.5996	4.5604	5.233	6.1714	7.1209
	$Y_{S\_SI}$	4.77E+16	7.17E+01	19.071	7.8524	5.4917	4.1402	2.4469
	$Z_{S\_SI}$	4.07E+15	3.35E+00	3.0561	4.1302	5.5186	7.8029	10.676
	$R_{S\_SI}$	6.74E+16	6.21E+01	18.899	8.0601	5.7851	4.6226	3.2449
	$Bearing\_SI$	709.58	71.503	4.4161	3.2162	4.1063	5.4522	7.1404
RMS error $\gamma_{ML}$ in meters	$X_{S\_ML}$	1.44E+08	2.85E+08	2.3264	1.5521	0.93432	0.55705	0.34377
	$Y_{S\_ML}$	2.45E+08	5.29E+08	14.03	4.4058	1.8069	0.71471	0.18799
	$Z_{S\_ML}$	6.98E+07	1.25E+08	1.6818	1.1783	0.75834	0.48799	0.32511
	$R_{S\_ML}$	2.93E+08	6.14E+08	13.983	4.4278	1.816	0.7184	0.18854
	$Bearing\_ML$	37.761	17.07	1.9484	1.0581	0.67287	0.41934	0.26998

Table 4. Effect of inter-sensor spacing on location estimation performance of the hybrid SI/ML method: error mean  $\mu$ , error variance  $\sigma^2$ , and RMS error  $\gamma$ . Results are based on 100 Monte Carlo runs.

Additional simulations are carried out to take into account the limited vertical inter-sensor spacing when the sensors are worn on soldiers or installed on vehicles. It is assumed that there is limited height of less than 2 m for the soldiers and less than 7 m for vehicles with elevated masts.

*a. Wearable Configuration*

To study the wearable configuration for the soldiers, another scenario is simulated to represent twelve soldiers ( $6 \times 2 \times 2$ ) with two sensors per soldier for different Z-spacing values of 1.0 m, 1.25 m, 1.5 m, 1.75 m and 2 m. Figure 21 shows the RMS error  $\gamma$  for the different Z-spacing values.

It can be seen that the RMS error decreases when the Z-spacing is increased. For example, the RMS errors for Zs readings at the ML stage decreased from 15 m to 8 m when the Z-spacing was increased from 1 m to 2 m; however, the RMS errors for Xs and Ys readings decreased slightly from 3 m and 8 m to 2 m and 7 m, respectively. Hence, it is recommended that the two sensors worn on the soldiers should be separated as far apart as practically possible; however, considering the constraint of the average height of a person ranging from 1.5 m to 2 m, the assumption of 1 m for the Z-spacing separation, say between the head to the waist level, is a reasonable assumption for a wearable configuration.

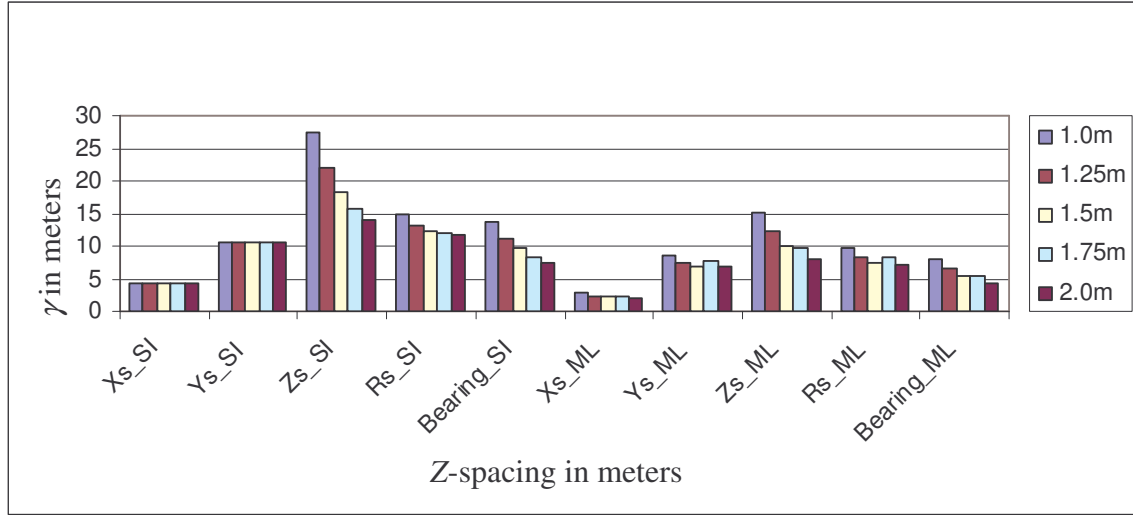


Figure 21. RMS error  $\gamma$  for different values of Z-spacing for  $6 \times 2 \times 2$  sensor nodes, representing a wearable configuration. Results are obtained by averaging output from 100 Monte Carlo simulations.

#### ***b. Vehicular Configuration***

A vehicular configuration can provide a larger vertical inter-sensor spacing compared to the wearable configuration. The second sensor can be mounted on an elevated mast to provide a larger sensor spacing in the Z direction and will improve the estimation accuracy.

To study the vehicular configuration, the scenario representing eight vehicles ( $4 \times 2 \times 2$ ) with two sensors installed vertically on each vehicle is simulated. The vehicles are spaced 10 m apart and the source is situated 100 m from the origin. The Z-spacing values are varied from 1 m to 7 m. Figure 22 shows the RMS error for different Z-spacing values.

When the Z-spacing is increased, the estimation accuracy increases. For example, with a Z-spacing of 3 m, the RMS error  $\gamma$  at the ML stage was 3 m, 14 m and 4 m for  $X_s$ ,  $Y_s$ , and  $Z_s$  readings, respectively; with a Z-spacing of 7 m, the RMS errors decreased to 2 m, 12 m and 2 m for  $X_s$ ,  $Y_s$ , and  $Z_s$  readings, respectively.



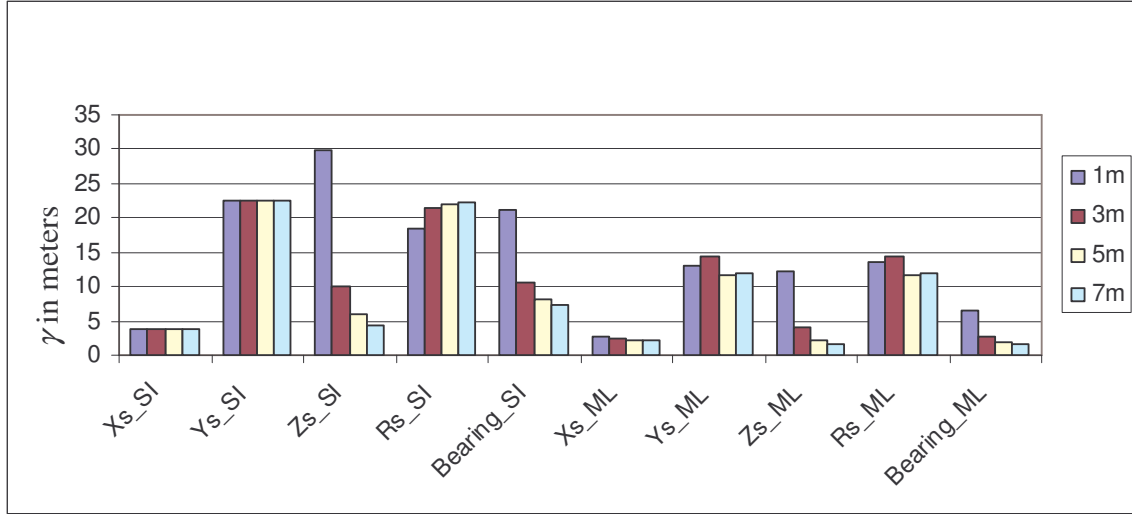


Figure 22. RMS error  $\gamma$  for different values of Z-spacing, from 1 m to 7 m, representing a vehicular configuration. Results are obtained by averaging output from 100 Monte Carlo simulations.

A similar scenario consisting of eight vehicles is repeated, but the simulation is carried out with different values of inter-vehicle spacing, from 10 m to 40 m. Figure 23 shows the RMS error for different vehicular spacing values.

It can be seen that the estimation accuracy can be improved by increasing the inter-vehicle spacing beyond 10 m. For example, for an inter-vehicle spacing of 10 m, the RMS error at the ML stage was 15 m for the  $R_s$  readings; for an inter-vehicle spacing of 40 m, the RMS error was significantly reduced to 4 m for the same reading.

In this scenario, however, wireless links that can cover a longer physical range will be needed. For instance, the IEEE 802.11 WLAN network with an effective range of up to 100 m can be used instead of the IEEE 802.15.4 WPAN that has an effective range of up to only 10 m.

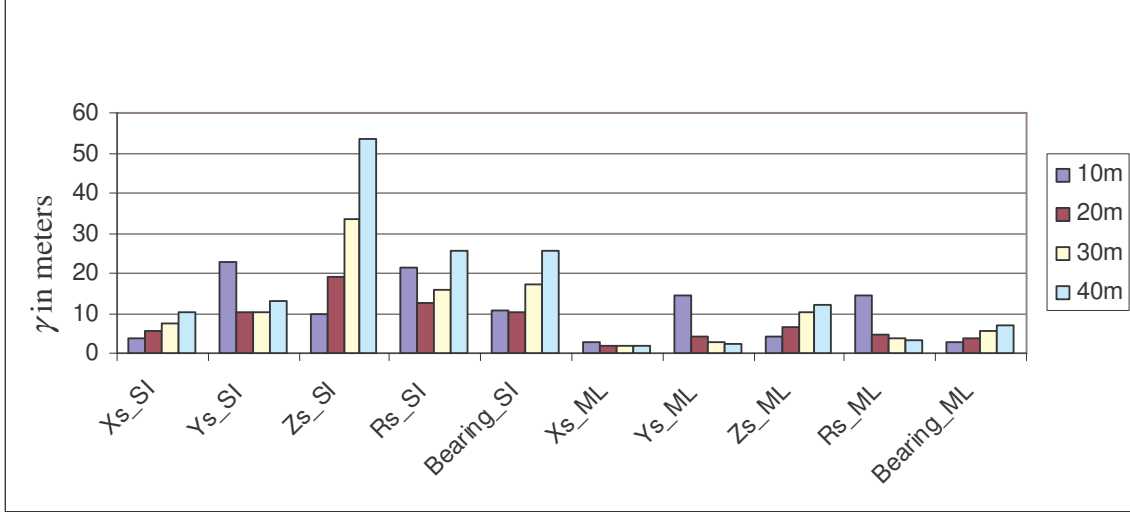


Figure 23. RMS error  $\gamma$  for different values of inter-vehicular spacing of 10 m, 20 m, 30 m, and 40 m, representing a vehicular configuration. Results are obtained by averaging output from 100 Monte Carlo simulations.

### 3. Effect of Topology

After studying the effect of the number of sensor nodes and the inter-sensor spacing, further simulations are carried out to find out a suitable sensor topology for the counter-sniper applications and the required number of sensors to be worn on soldiers. To study the effect of topology on the location estimation performance, different two-dimensional ( $4 \times 2 \times 1$  and  $8 \times 2 \times 1$ ) and three-dimensional topologies ( $4 \times 2 \times 2$  and  $4 \times 2 \times 3$ ) are simulated. Figure 24 shows four different simulated topologies used in the study. The  $4 \times 2 \times 1$  and  $8 \times 2 \times 1$  topologies refer to the layout of eight and sixteen sensors on the  $XY$  plane, respectively. The  $4 \times 2 \times 2$  and  $4 \times 2 \times 3$  topologies refer to the layout of eight sensor columns with two sensors and three sensors, respectively, along the  $Z$  axis. Each sensor is separated by a distance of 10 m.

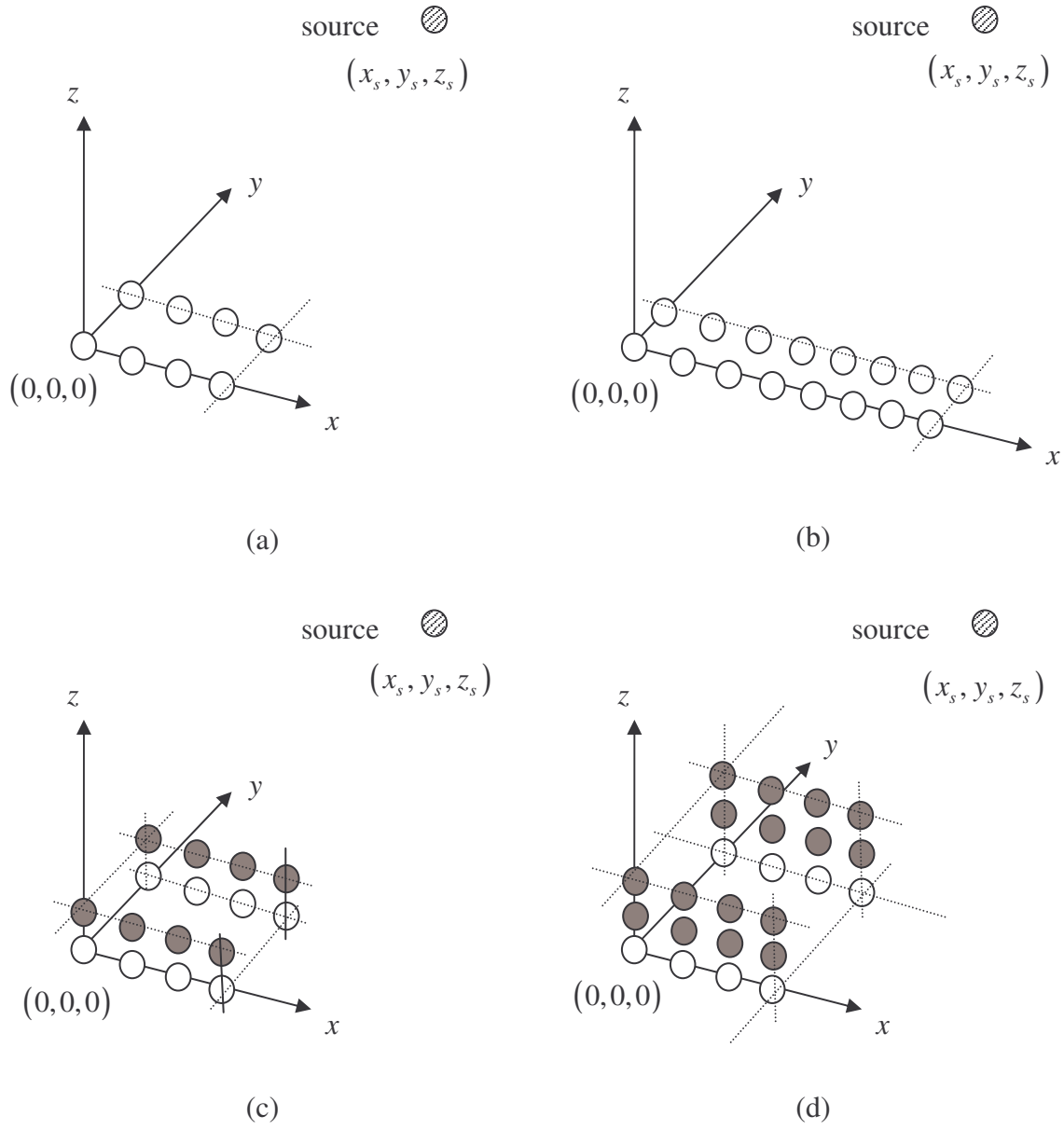


Figure 24. Different sensor topologies: (a)  $4 \times 2 \times 1$ , (b)  $8 \times 2 \times 1$ , (c)  $4 \times 2 \times 2$  and (d)  $4 \times 2 \times 3$ . White and grey circles represent sensors that are placed in the two-dimensional  $XY$  and three-dimensional  $XYZ$  planes, respectively.

Figure 25 shows the RMS errors for the four sensor topologies considered. Simulation results indicate that although the estimation errors are low in the  $X$  direction for the case of eight sensors lying on the  $XY$  plane (i.e.,  $4 \times 2 \times 1$  topology), the estimation

errors in the  $Y$  and  $Z$  directions are relatively large. For example, RMS error of the  $X_s$ ,  $Y_s$  and  $Z_s$  values at the ML stage for the  $4 \times 2 \times 1$  topology was 10 m, 40 m and 30 m, respectively.

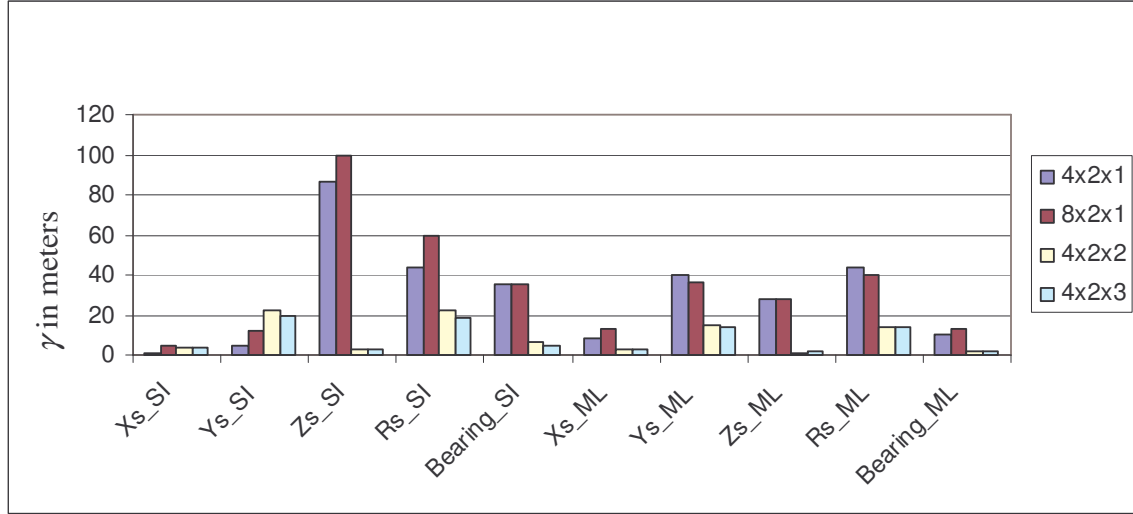


Figure 25. RMS error  $\gamma$  for different two-dimensional ( $4 \times 2 \times 1$  and  $8 \times 2 \times 1$ ) and three-dimensional topologies ( $4 \times 2 \times 2$  and  $4 \times 2 \times 3$ ). Results are obtained by averaging output from 100 Monte Carlo simulations.

The same observation of large estimation errors in the  $Y$  and  $Z$  directions can be seen when the number of sensors lying on the  $XY$  plane is increased from eight to sixteen (i.e.,  $8 \times 2 \times 1$  topology). For example, the RMS error for the  $X_s$ ,  $Y_s$  and  $Z_s$  values at the ML stage for the  $8 \times 2 \times 1$  topology was 15 m, 35 m and 30 m, respectively. However, it is observed that when the number of sensor nodes in the  $Z$  direction is increased (i.e.,  $4 \times 2 \times 2$  and  $4 \times 2 \times 3$  topologies), there is significant improvement in the estimation accuracy in the all three directions. For example, the  $4 \times 2 \times 1$  and  $8 \times 2 \times 1$  topologies produce the largest error of 30 m in the  $Z_s$  readings at the ML stage while the  $4 \times 2 \times 2$  and  $4 \times 2 \times 3$  topologies produce the smallest error of 3 m in the  $Z_s$  readings. Hence, it is recommended that the sensor topology should be well represented in all three directions to obtain good estimation accuracy in all three dimensions.

Another scenario is carried out to represent topologies for sensors worn on soldiers. For wearable sensors, it is assumed that there is a limited height of less than 2 m

where the sensors can be worn on the soldier's foot and helmet. The simulation is carried out by having one topology of two wearable sensors spaced 1 m to 1.5 m apart and another topology of three wearable sensors spaced 0.5 m to 0.75 m apart.

Figure 26 shows the RMS error  $\gamma$  for different number of vertical sensors per soldier: two wearable sensors spaced 1 m to 1.5 m apart ( $6 \times 2 \times 2$ ) and three wearable sensors spaced 0.5 m to 0.75 m apart ( $6 \times 2 \times 3$ ). It can be seen that the estimation accuracy is comparable for the two-sensor ( $6 \times 2 \times 2$ ) and three-sensor wearable configurations ( $6 \times 2 \times 3$ ). For example, the topologies of  $6 \times 2 \times 2$  (Z-spacing = 1 m) and  $6 \times 2 \times 3$  (Z-spacing = 0.5 m) produced similar RMS errors of 3 m, 8 m and 15 m for  $X_s$ ,  $Y_s$  and  $Z_s$  readings, respectively, at the ML stage. Similarly, the topologies of  $6 \times 2 \times 2$  (Z-spacing = 1.5 m) and  $6 \times 2 \times 3$  (Z-spacing = 0.75 m) produced similar RMS errors of 3 m, 7 m and 11 m for  $X_s$ ,  $Y_s$  and  $Z_s$  readings, respectively. Thus, it is recommended that two sensors per soldier will be sufficient.

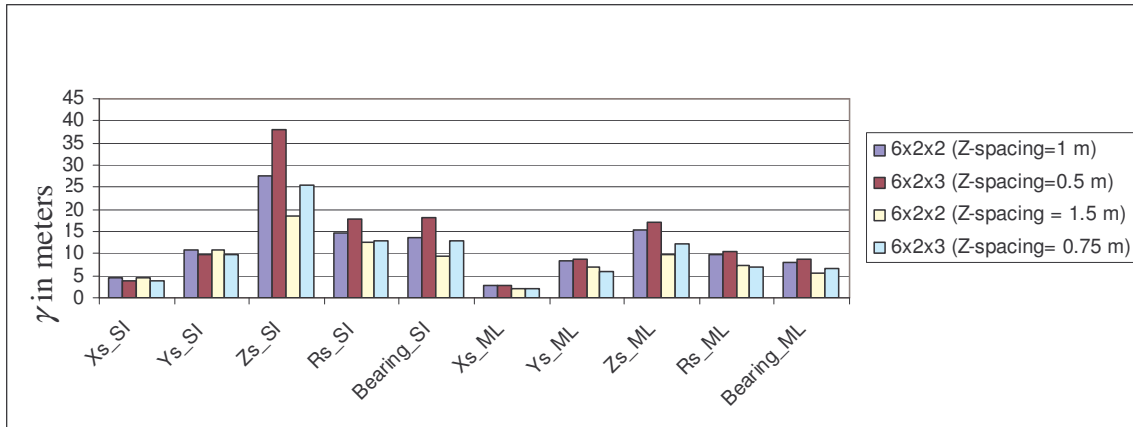


Figure 26. RMS error  $\gamma$  for two-sensor ( $6 \times 2 \times 2$  with Z-spacing of 1 m and 1.5 m) and three-sensor ( $6 \times 2 \times 3$  with Z-spacing of 0.5 m and 0.75 m) topologies, representing wearable configuration. Results are obtained by averaging output from 100 Monte Carlo simulations.

#### 4. Effect of Noise

Measurement noise is expected to have a significant effect on the estimation accuracy [14]. The variance in acoustic travel time  $\sigma_t^2$  along a ray path from source to receiver is proportional to the propagation distance  $R_s$  as given by [3]

$$\sigma_t^2 = 0.4 \chi^2 \frac{R_s L}{v^2}$$

where  $L$  represents the correlation length of atmospheric turbulence,  $v$  is the speed of sound and  $\chi^2$  is the mean-squared sound-speed fluctuations near the ground. However, the proportionality property is valid only for short distances of less than 60 m. A higher order approximation is required to provide a more realistic estimation. In this study, the RDOA noise variance is modeled as a second-order approximation

$$\sigma_n^2 = aR_s^2$$

where  $a$  is a constant that is set to 0.01 for the study.

To study the effect of noise on the location estimation performance, a scenario consisting of 24 sensor nodes ( $6 \times 2 \times 2$ ), as shown in Figure 27, with a 10-m spacing between adjacent sensors is simulated. The source is placed 100 m from the origin.

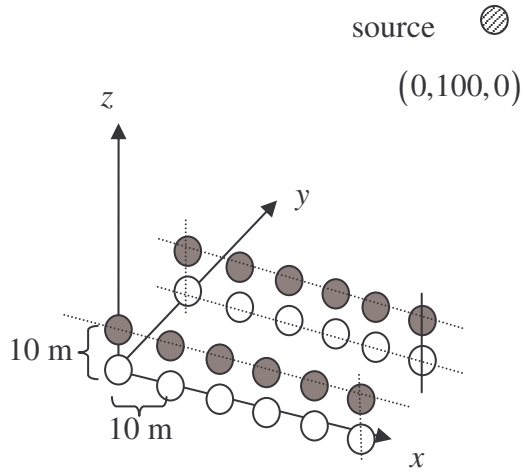
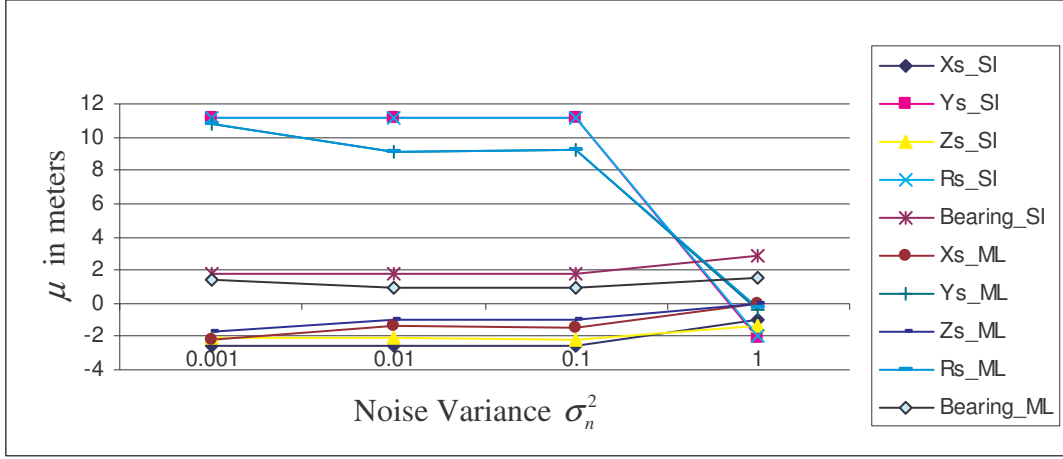
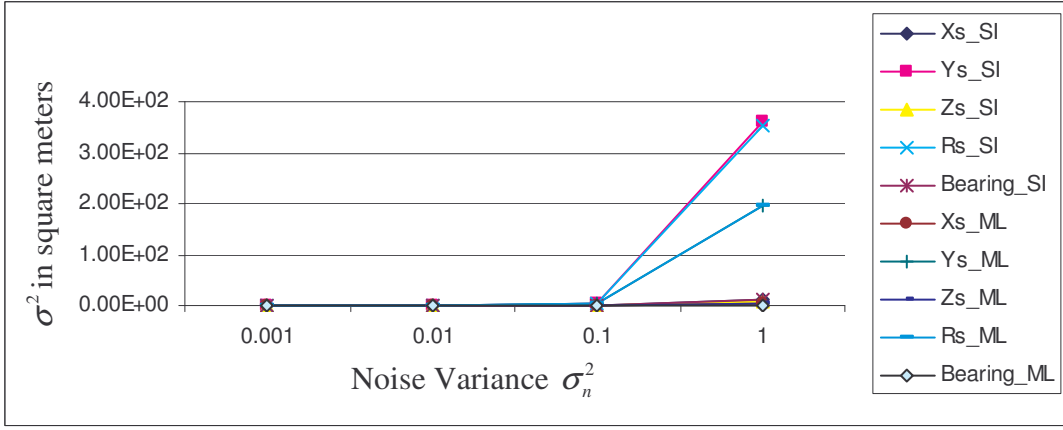


Figure 27. Simulated scenario of 24 sensor nodes ( $6 \times 2 \times 2$ ) with a 10-m spacing between adjacent sensors is simulated. The source is placed 100 m from the origin.

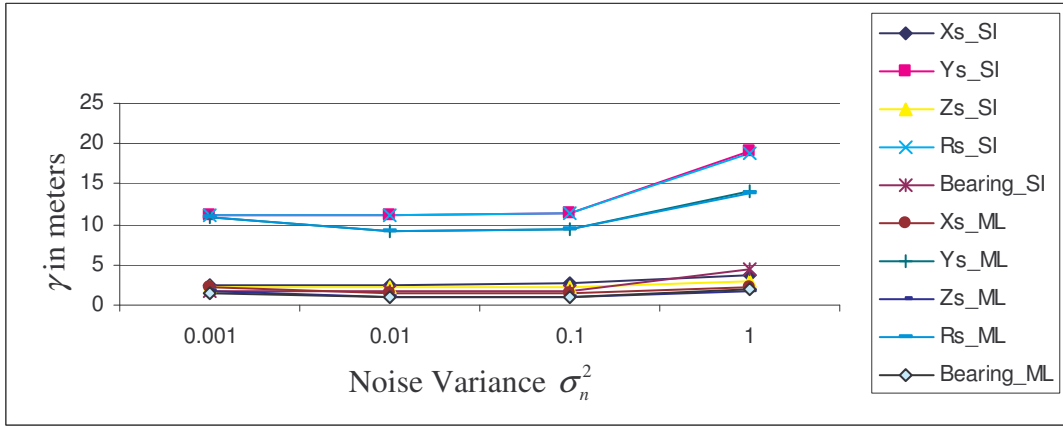
Figure 28 and Table 5 show the error mean  $\mu$ , error variance  $\sigma^2$ , and RMS error  $\gamma$  for different noise levels.



(a)



(b)



(c)

Figure 28. Effect of noise on location estimation performance of the hybrid SI/ML method with different noise variance  $\sigma_n^2$  for: (a) error mean  $\mu$ , (b) error variance  $\sigma^2$ , and (c) RMS error  $\gamma$ , representing a  $6 \times 2 \times 2$  topology. Results are based on 100 Monte Carlo runs.

	Noise variance $\sigma_n^2$	0.001	0.01	0.1	1
Error mean $\mu_{SI}$ in meters	$Xs\_SI$	-2.5658	-2.5682	-2.5822	-1.021
	$Ys\_SI$	11.133	11.141	11.115	-2.0383
	$Zs\_SI$	-2.1288	-2.1309	-2.1485	-1.3407
	$Rs\_SI$	11.183	11.191	11.168	-1.8955
	$Bearing\_SI$	1.7183	1.7198	1.7261	2.8112
Error mean $\mu_{ML}$ in meters	$Xs\_ML$	-2.1565	-1.4044	-1.4486	0.007947
	$Ys\_ML$	10.818	9.0713	9.2698	-0.37713
	$Zs\_ML$	-1.6793	-0.95559	-0.97037	-0.01764
	$Rs\_ML$	10.854	9.0848	9.2844	-0.32973
	$Bearing\_ML$	1.4118	0.89127	0.91088	1.535
Error variance $\sigma_{SI}^2$ in square meters	$Xs\_SI$	2.57E-05	0.002569	0.25342	11.914
	$Ys\_SI$	0.000386	0.038694	3.8292	359.54
	$Zs\_SI$	1.84E-05	0.001845	0.18198	7.5425
	$Rs\_SI$	0.000394	0.039445	3.9012	353.59
	$Bearing\_SI$	9.72E-06	0.000973	0.09733	11.599
Error variance $\sigma_{ML}^2$ in square meters	$Xs\_ML$	2.66E-01	0.04107	0.1096	5.4121
	$Ys\_ML$	1.837	1.1165	3.4264	196.71
	$Zs\_ML$	2.88E-01	0.02666	0.063778	2.828
	$Rs\_ML$	1.8589	1.1228	3.4485	195.4
	$Bearing\_ML$	1.39E-01	0.017059	0.041712	1.4399
RMS error $\gamma_{SI}$ in meters	$Xs\_SI$	2.5658	2.5687	2.6308	3.5996
	$Ys\_SI$	11.133	11.143	11.286	19.071
	$Zs\_SI$	2.1288	2.1313	2.1905	3.0561
	$Rs\_SI$	11.183	11.193	11.341	18.899
	$Bearing\_SI$	1.7183	1.7201	1.7541	4.4161
RMS error $\gamma_{ML}$ in meters	$Xs\_ML$	2.2173	1.419	1.4859	2.3264
	$Ys\_ML$	10.902	9.1327	9.4528	14.03
	$Zs\_ML$	1.7629	0.96944	1.0027	1.6818
	$Rs\_ML$	10.939	9.1464	9.4683	13.983
	$Bearing\_ML$	1.4603	0.90079	0.9335	1.9484

Table 5. Effect of noise on the location estimation performance of the hybrid SI/ML method with different noise variance  $\sigma_n^2$  for: error mean  $\mu$ , error variance  $\sigma^2$ , and RMS error  $\gamma$ , representing a 6×2×2 topology. Results are obtained by averaging output from 100 Monte Carlo simulations.

It can be seen that as the noise variance  $\sigma_n^2$  increases, the error variance  $\sigma^2$  increases. For example, the error variance  $\sigma^2$  for the  $Rs$  value at the ML stage increased from 1.1 m<sup>2</sup> to 3.4 m<sup>2</sup> when the noise variance  $\sigma_n^2$  increased from 0.1 to 1.



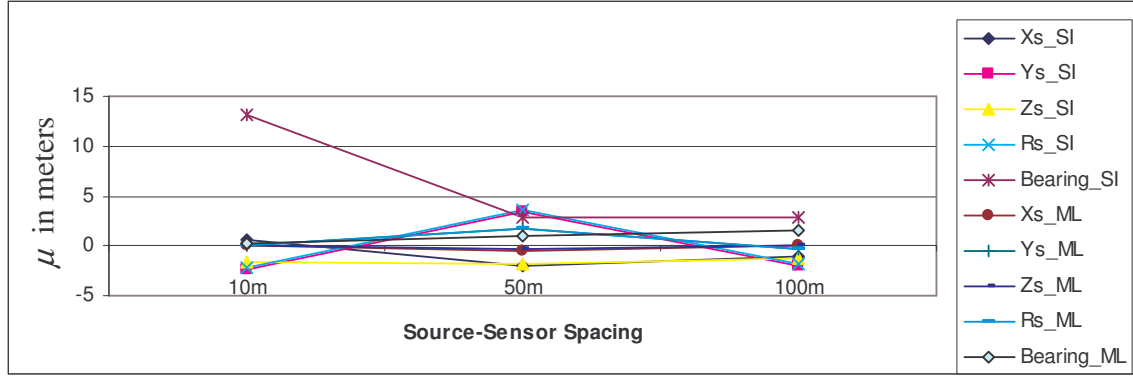
Although it is expected that a noisier environment will lead to greater estimation errors, it is interesting to note that at high noise levels (i.e.,  $\sigma_n^2 = 1$ ), ML actually produces an error mean that is better than for low noise levels (i.e.,  $\sigma_n^2 = 0.001, 0.01$  or  $0.1$ ). For example, the error mean for the  $R_s$  values for the ML stage are 11 m and -2 m for  $\sigma_n^2$  values of 0.1 and 1, respectively. This anomaly is likely due to the inaccurate SI value that is used as the initial value for the ML stage. At low noise levels, the SI stage introduces large bias of approximately 11 m and leads to similarly large errors of approximately 10 m for the ML stage. The smaller bias of 2 m introduced by SI at high noise levels actually leads to better estimation accuracy in the ML stage.

## 5. Effect of Source-Sensor Distance

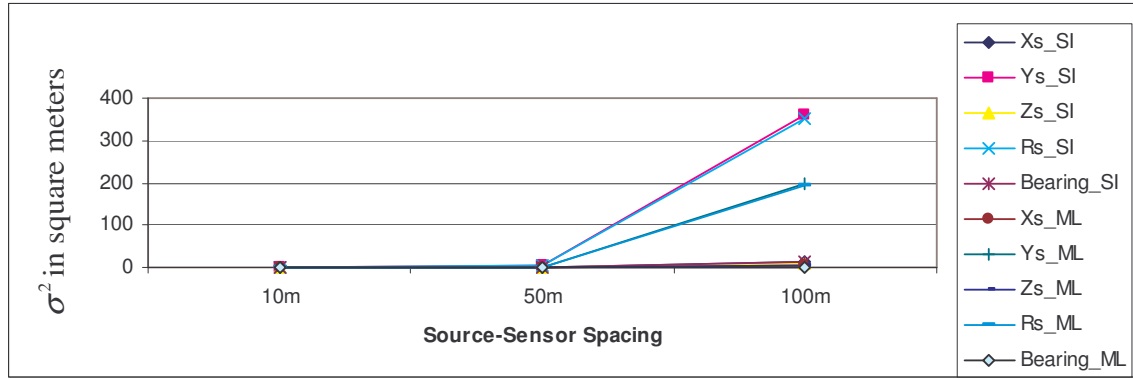
To study the effect of the source-sensor distance on the location estimation performance, a scenario consisting of 24 sensor nodes ( $6 \times 2 \times 2$ ) is simulated. The distance between the source and the sensor is varied from 10 m to 200 m. Figure 29 and Table 6 show the error mean  $\mu$ , error variance  $\sigma^2$ , and RMS error  $\gamma$  for the various source-sensor distances in this range.

As the source-sensor distance increases, the error variance  $\sigma^2$  increases. It is seen that the error variance of the SI method in the first stage increases much rapidly than that in the ML stage. For example, at the first SI stage, the error variance of  $R_s$  value increases from  $4 \text{ m}^2$  to  $354 \text{ m}^2$  when the source-sensor distance is increased from 50 m to 100 m; the error variance at the ML stage increases from  $2 \text{ m}^2$  to  $195 \text{ m}^2$ , correspondingly.

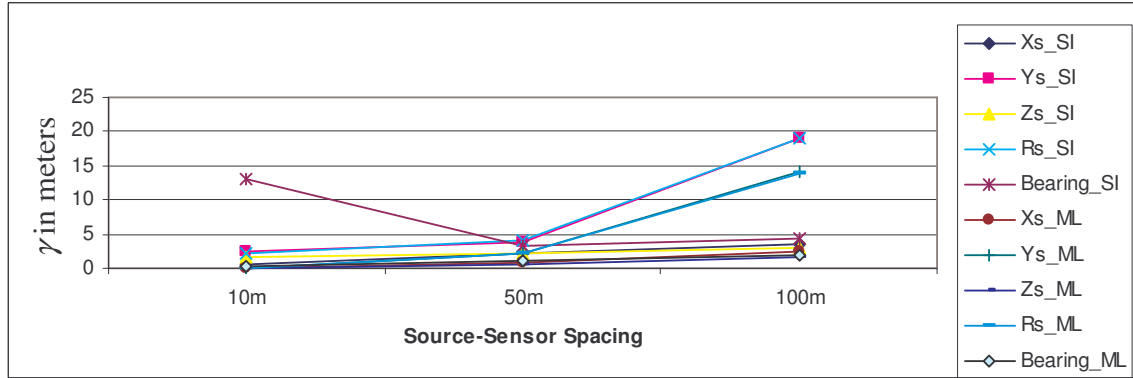
However, when the source-sensor distance increases from 150 m and beyond, the ML method produces very divergent results due to the erroneous estimates provided by the SI method and are not shown in Figure 28.



(a)



(b)



(c)

Figure 29. Effect of source-sensor distance on location estimation performance of the hybrid SI/ML method: (a) error mean  $\mu$ , (b) error variance  $\sigma^2$ , and (c) RMS error  $\gamma$ , representing a  $6 \times 2 \times 2$  topology. Results are obtained by averaging output from 100 Monte Carlo simulations. Readings for 150 m and beyond are not shown due to erroneous results.

	Source-sensor distance	10 m	50 m	100 m	150 m	200 m
Error mean $\mu_{SI}$ in meters	$Xs\_SI$	0.55436	-1.9831	-1.021	3.6574	7.7222
	$Ys\_SI$	-2.3537	3.4415	-2.0383	-48.569	-112.68
	$Zs\_SI$	-1.6988	-1.8335	-1.3407	1.7466	4.6552
	$Rs\_SI$	-2.1474	3.5276	-1.8955	-45.186	-99.574
	$Bearing\_SI$	13.165	2.8987	2.8112	16.813	42.603
Error mean $\mu_{ML}$ in meters	$Xs\_ML$	-0.01412	-0.54358	0.007947	1.21E+08	2.76E+07
	$Ys\_ML$	0.005905	1.7556	-0.37713	3.36E+08	4.72E+08
	$Zs\_ML$	-0.0134	-0.38831	-0.01764	-7.11E+07	-1.56E+08
	$Rs\_ML$	0.005981	1.7648	-0.32973	4.27E+08	5.73E+08
	$Bearing\_ML$	0.15755	0.93126	1.535	5.4505	10.156
Error variance $\sigma_{SI}^2$ in square meters	$Xs\_SI$	0.004201	1.2665	11.914	36.192	47.508
	$Ys\_SI$	0.005741	3.5715	359.54	3341.5	7866.5
	$Zs\_SI$	0.001391	0.90292	7.5425	18.249	23.135
	$Rs\_SI$	0.005977	3.7969	353.59	2707.9	5533.6
	$Bearing\_SI$	0.000324	1.9415	11.599	1240	3297.6
Error variance $\sigma_{ML}^2$ in square meters	$Xs\_ML$	0.000607	0.32603	5.4121	2.18E+18	5.71E+17
	$Ys\_ML$	0.000151	2.001	196.71	3.46E+18	1.32E+18
	$Zs\_ML$	0.000558	0.21051	2.828	1.70E+17	1.96E+17
	$Rs\_ML$	0.000149	2.0198	195.4	5.75E+18	2.00E+18
	$Bearing\_ML$	0.025758	0.28883	1.4399	86.278	144.19
RMS error $\gamma_{SI}$ in meters	$Xs\_SI$	0.55813	2.2802	3.5996	7.0404	10.351
	$Ys\_SI$	2.3549	3.9262	19.071	75.501	143.4
	$Zs\_SI$	1.6992	2.0651	3.0561	4.6151	6.6938
	$Rs\_SI$	2.1487	4.03	18.899	68.918	124.29
	$Bearing\_SI$	13.165	3.2162	4.4161	39.021	71.503
RMS error $\gamma_{ML}$ in meters	$Xs\_ML$	0.0284	0.78836	2.3264	1.48E+09	7.56E+08
	$Ys\_ML$	0.013616	2.2546	14.03	1.89E+09	1.24E+09
	$Zs\_ML$	0.027152	0.60108	1.6818	4.18E+08	4.70E+08
	$Rs\_ML$	0.013599	2.2659	13.983	2.44E+09	1.53E+09
	$Bearing\_ML$	0.2249	1.0752	1.9484	10.77	15.727

Table 6. Effect of source-sensor distance on location estimation performance of the hybrid SI/ML method: error mean  $\mu$ , error variance  $\sigma^2$ , and RMS error  $\gamma$ , representing a 6×2×2 topology. Results are obtained by averaging output from 100 Monte Carlo simulations.

Another scenario is carried out to simulate the effect of source-sensor distance on the location estimation performance for a group of soldiers equipped with two sensors each. A scenario consisting of 24 sensors ( $6 \times 2 \times 2$ ) is simulated to represent twelve soldiers who are individually equipped with two sensors that are spaced 1 m apart on their body. Each soldier is stationed 10 m apart, and the source is situated 50 m to 200 m from the origin. Figure 30 shows the RMS error  $\gamma$  for the  $6 \times 2 \times 2$  soldier configuration with different source-sensor distances: 50 m, 100 m, 150 m and 200 m.

It is seen that when the source-sensor distance increases, the RMS error  $\gamma$  increases. For example, at a source-sensor distance of 100 m, the RMS error  $\gamma$  for  $X_s$ ,  $Y_s$  and  $Z_s$  readings at the ML stage is 3 m, 8 m and 15 m, respectively; at a source-sensor distance of 200 m, the RMS error  $\gamma$  for  $X_s$ ,  $Y_s$  and  $Z_s$  readings at the ML stage is 8 m, 45 m and 32 m, respectively.

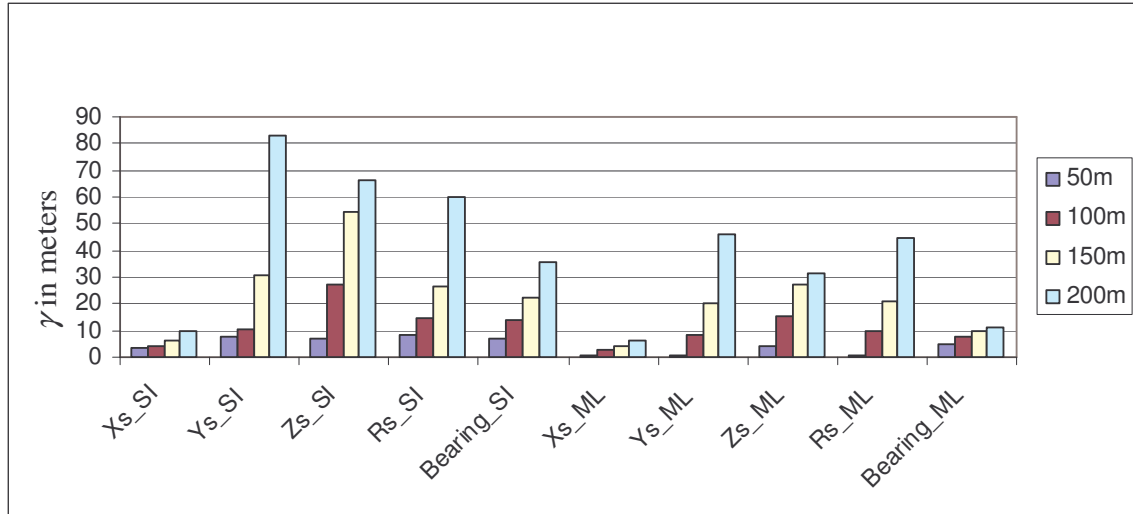


Figure 30. RMS error  $\gamma$  for different values of source-sensor distances: 50 m, 100 m, 150 m and 200 m, representing a  $6 \times 2 \times 2$  wearable configuration. Results are obtained by averaging output from 100 Monte Carlo simulations.

## 6. Effect of Node Failures

Node failures can occur when a sensor's battery runs out or the sensor may be asleep when the source is detected. The scenario representing twelve soldiers with two

sensors each ( $6 \times 2 \times 2$ ) is studied. Each soldier is stationed 10 m apart, and the source is 100 m from the origin. Figure 31 shows the RMS error as a function of the number of sensor node failures.

The RMS error  $\gamma$  steadily increases as the number of sensor node failures increases from two to twelve. For example, the RMS error for the  $R_s$  value increases gradually from 10 m to 20 m when the number of sensor node failures increases from zero to ten. This demonstrates the advantage of having distributed wireless sensor networks where sensor node failures lead to a graceful degradation of performance and not a sudden system failure. Note that drastic increase in the RMS error  $\gamma$  at the SI stage is observed only when there are twelve or more sensor node failures (i.e., 50 % sensor node failure). At such a high failure rate, the SI method used in the first stage of the hybrid SI/ML method gives a large RMS error of 50 m for the  $R_s$  value, but the ML method in the second stage is able to tolerate the errors and produced RMS errors for the  $R_s$  value of less than 10 m.

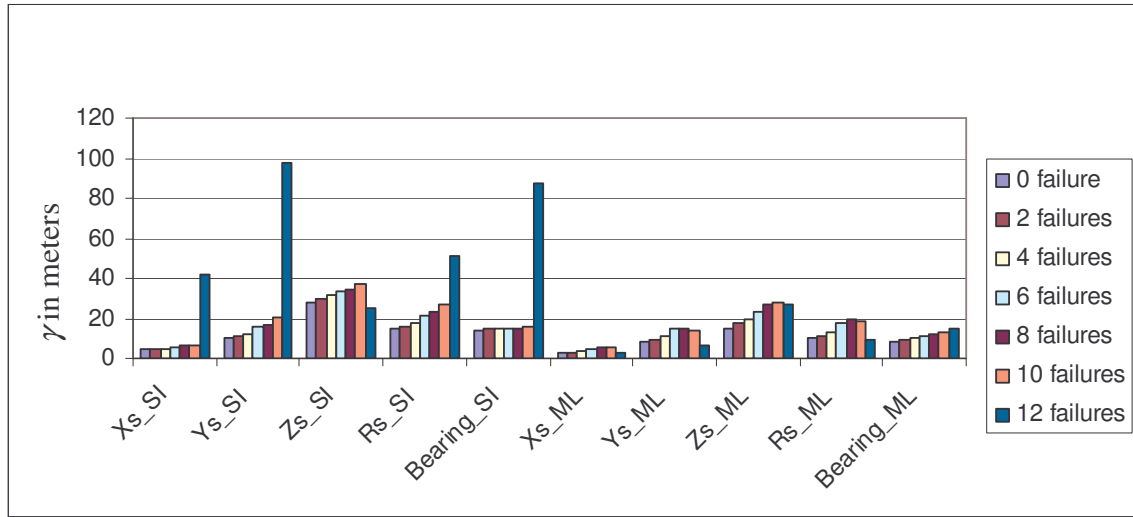


Figure 31. RMS error  $\gamma$  as the function of the number of sensor node failures, representing a  $6 \times 2 \times 2$  wearable configuration. Results are obtained by averaging output from 100 Monte Carlo simulations.

## 7. Effect of Location Perturbations

In field deployment, it is expected that there will be some perturbation (or slight deviation) in the sensor locations as perfectly straight line troop formation or exact symmetry is usually not possible. This perturbation effect on location estimation performance is studied by introducing some degree of randomness to the sensor positions. The standard deviation of the random distance between soldiers is varied from 0.01 to 1; the standard deviation of the two sensor locations on a soldier is set to 0.01. Figure 32 shows the RMS error  $\gamma$  for different values of standard deviations of location perturbations.

It is seen that RMS error  $\gamma$  is similar for low and high standard deviations of location perturbation. For example, the RMS error for the  $R_s$  value is between 7 m to 9 m for the ML method at the second stage of the hybrid SI/ML algorithm for the various levels of location perturbation standard deviations. This shows that location perturbation has limited effect on the estimation accuracy. This clearly illustrates the flexibility of the network configuration and demonstrates the suitability for potential field deployment.

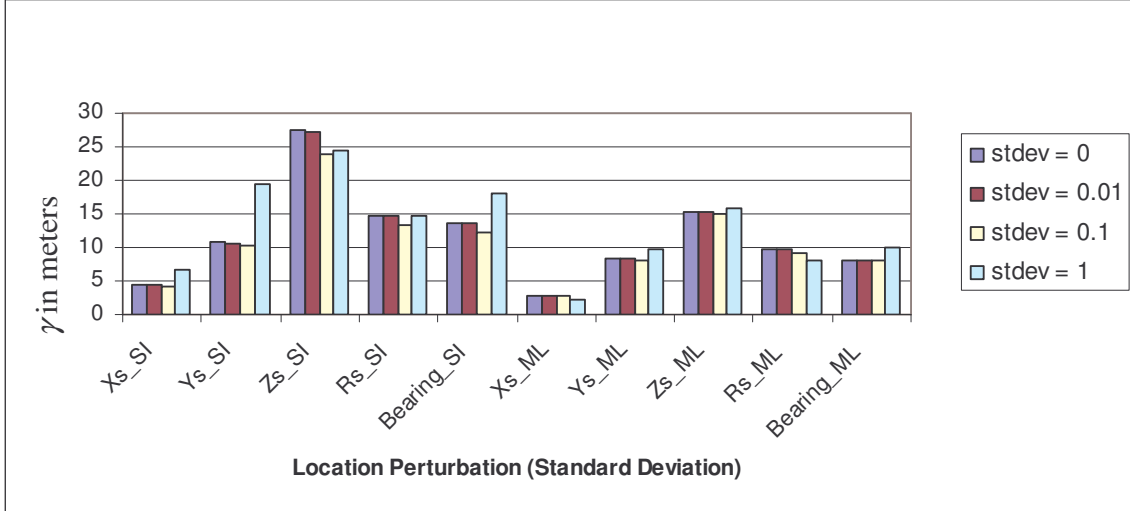


Figure 32. RMS error  $\gamma$  for different values of standard deviations of location perturbations, representing a  $6 \times 2 \times 2$  wearable configuration

### C. WIRELESS NETWORK SIMULATION

The wireless network simulation is carried out using NS-2 simulator, a discrete event simulator suitable for networking research. The wireless extension and the 802.15.4 extension [19] are used to conduct the studies on scenarios using an IEEE 802.11-based wireless local area network (WLAN) and an IEEE 802.15.4-based wireless personal area network (WPAN). Figure 33 shows the protocol architecture of the NS-2 wireless extension to support WPAN simulation.

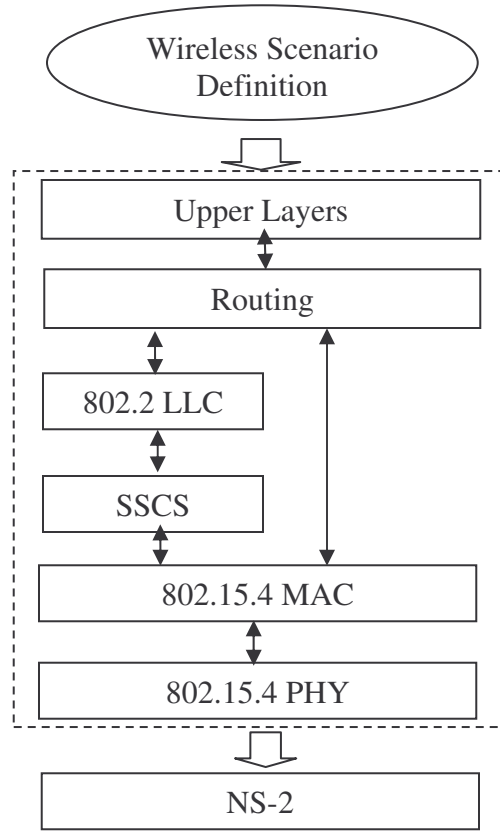


Figure 33. The protocol architecture of the IEEE 802.15.4 WPAN extension in NS-2 (from [8]).

A scenario of a wireless sensor network consisting of 26 sensor nodes situated over a 50 m×50 m area is simulated using NS-2. Figure 34 shows the layout of the sensors defined for the scenario used for the simulation. The traffic scenario of twelve sensor nodes (#1 to #12) sending Constant Bit Rate (CBR) traffic to a central node (#19) at the same time is simulated. The Adhoc On-demand Distance Vector (AODV) routing

protocol [20] is run on top of the 802.15.4 MAC and PHY layers to study the performance of WPAN networks. Similarly, the AODV routing protocol is run on top of 802.11 MAC and PHY layer to study the performance of WLAN networks.

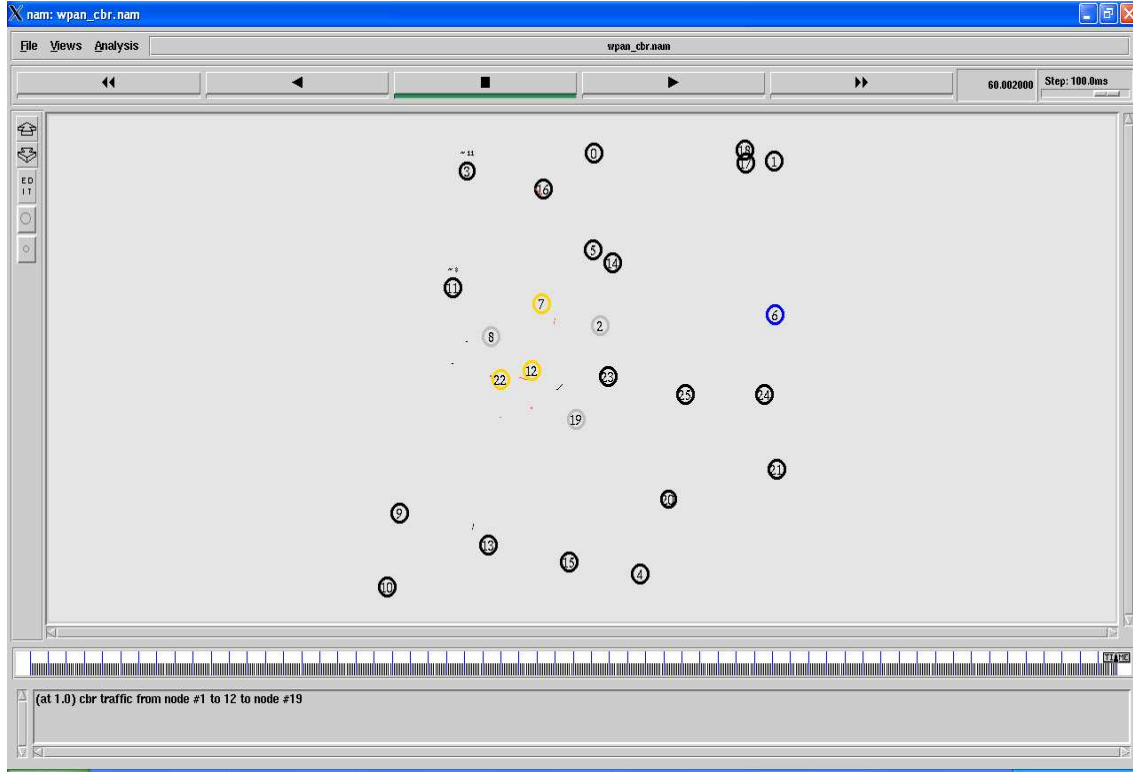


Figure 34. NS-2 WPAN and WLAN Simulation Scenario: 26 sensor nodes in a  $50 \times 50 \text{ m}^2$  area. The Time Interval Length (TIL) used in the simulation is equal to one second.

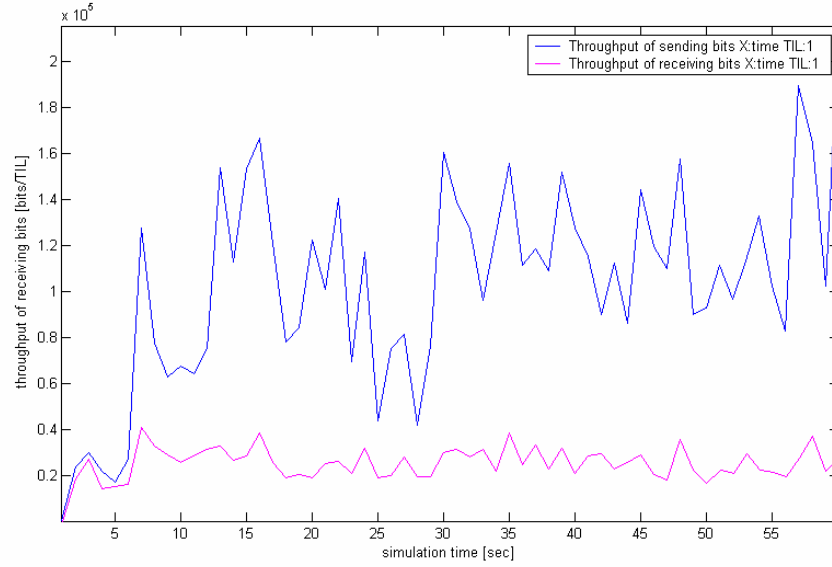
### 1. Sending/Receiving Throughput

Figure 35 shows the sending and receiving throughput for WPAN and WLAN networks. The Time Interval Length (TIL) used in the simulation is equal to one second. The average sending throughput refers to the average throughput of nodes 1 to 12 that are sending CBR traffic to central node 19; the average receiving throughput refers to the average throughput received by node 19.

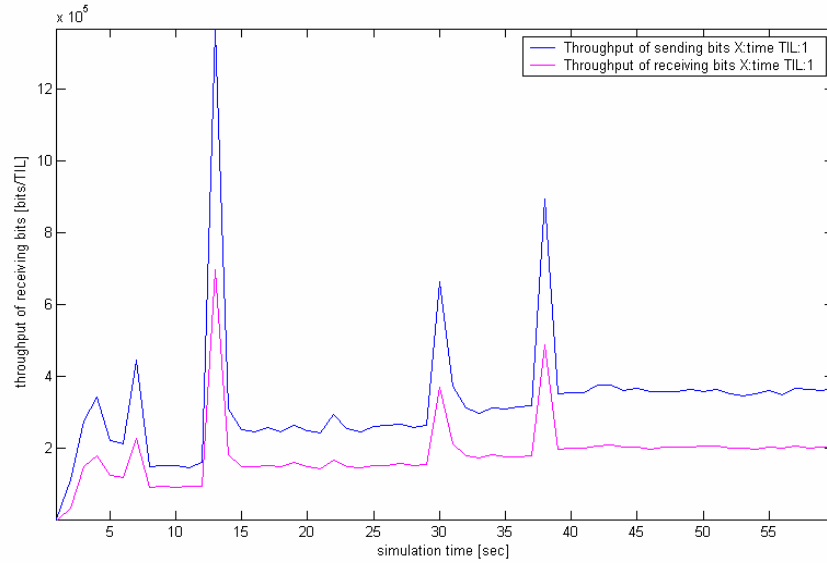
For WPAN networks, the average sending throughput is approximately 100 kbps and the receiving throughput is approximately 20 kbps. It is observed that the WLAN



network has better throughput than WPAN network. For WLAN networks, the average sending throughput is approximately 300 kbps and the receiving throughput is approximately 200 kbps.



(a)



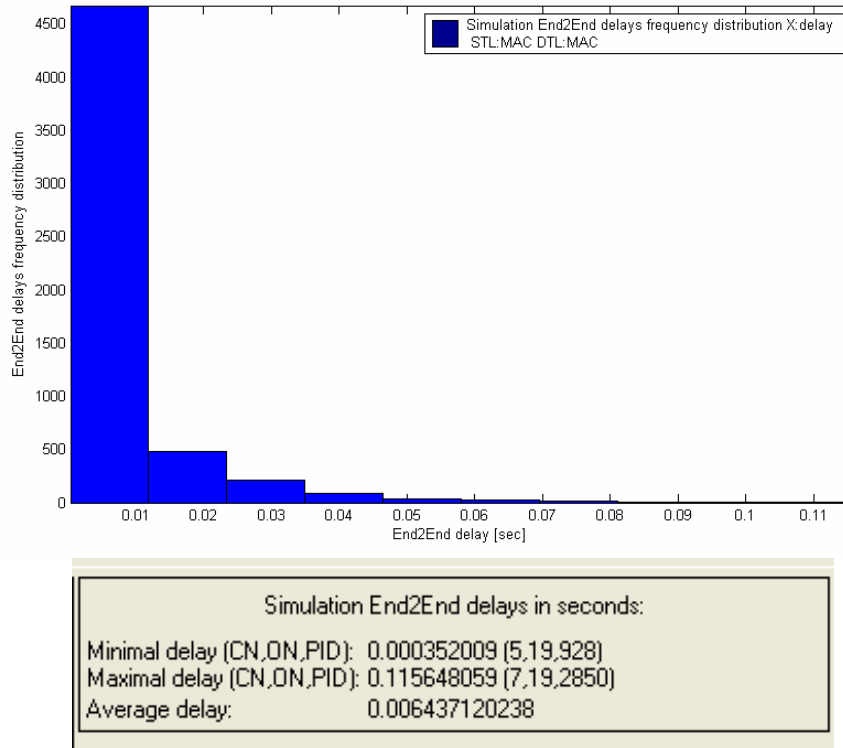
(b)

Figure 35. Sending and Receiving Throughput of: (a) WPAN and (b) WLAN. The Time Interval Length (TIL) used in the simulation is equal to one second. NS-2 simulation of a 26-node network operating over an area of  $50 \times 50 \text{ m}^2$ .

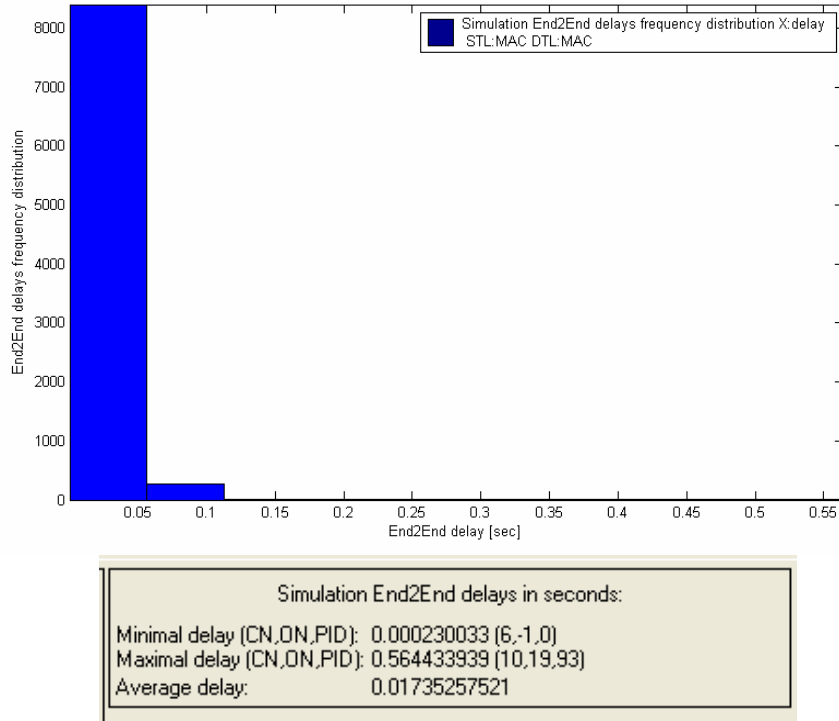
## 2. End-to-End Delay

Figure 36 shows the histograms and the summary statistics for the end-to-end delay for the WPAN and WLAN networks. For WPAN networks, approximately 90 % of the traffic has end-to-end delay of less than 10 ms. The average WPAN end-to-end delay is 6.4 ms. The minimum WPAN delay is 0.35 ms and the maximum delay is 115 ms.

It is observed that the end-to-end delay in the WLAN network is slightly higher than that in the WPAN network. For WLAN networks, approximately 97 % of the traffic has end-to-end delay of less than 50 ms. The average WLAN end-to-end delay is 17 ms. The minimum WLAN delay is 0.2 ms and the maximum delay is 564 ms. This observation of lower end-to-end delay in the WPAN networks compared to the WLAN networks is consistent with the results of the WPAN performance study performed by Zheng [19].



(a)



(b)

Figure 36. End-to-End delay for: (a) WPAN and (b) WLAN. NS-2 simulation of a 26-node network operating over an area of  $50 \times 50 \text{ m}^2$ .

### 3. Packet Size

Figure 37 shows the simulation summary statistics for WPAN and WLAN networks. The average WPAN packet size is 51.37 bytes with a minimum packet size of 5 bytes and a maximum packet size of 111 bytes. The WLAN networks have a similar packet size as WPAN networks. The average WLAN packet size is 57.51 bytes with a minimum packet size of 28 bytes and a maximum packet size of 142 bytes.

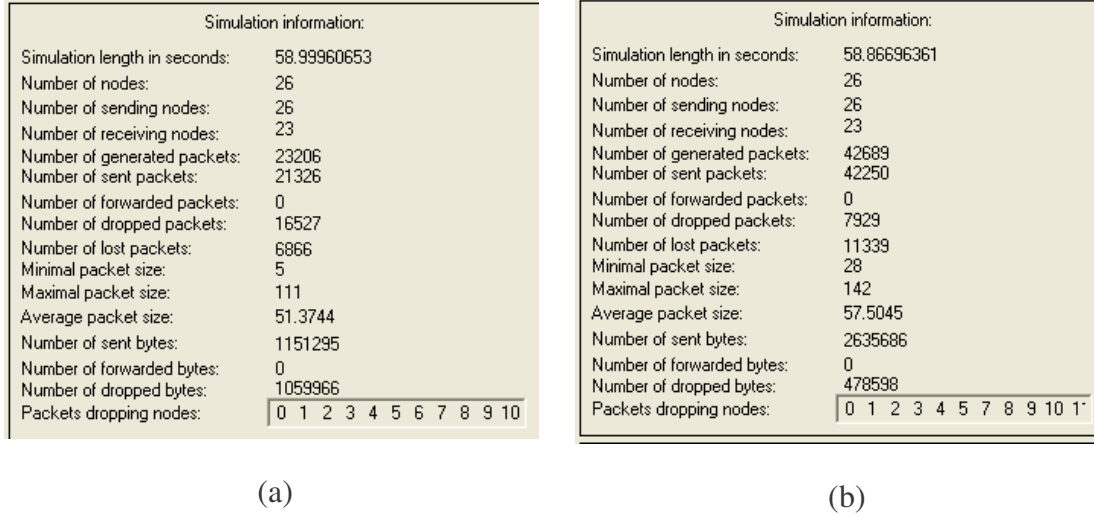
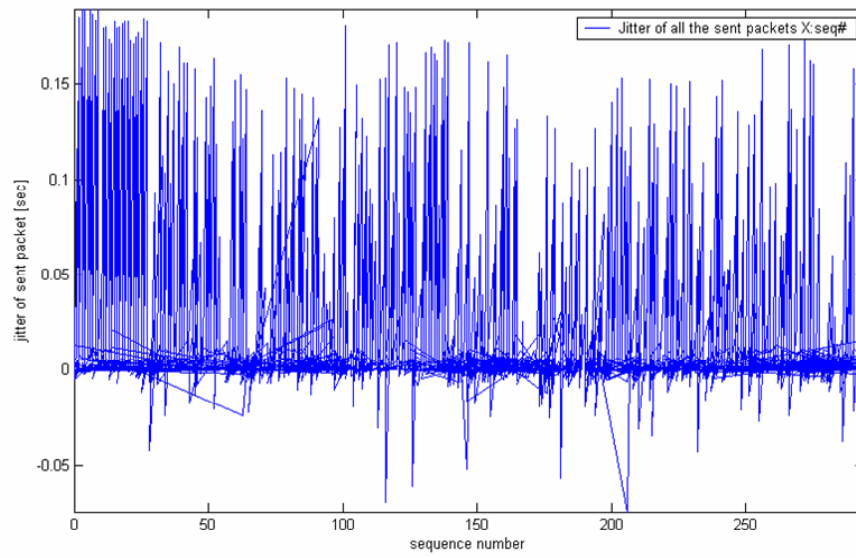


Figure 37. Simulation summary statistics for: (a) WPAN and (b) WLAN networks. NS-2 simulation of a 26-node network operating over an area of  $50 \times 50 \text{ m}^2$ .

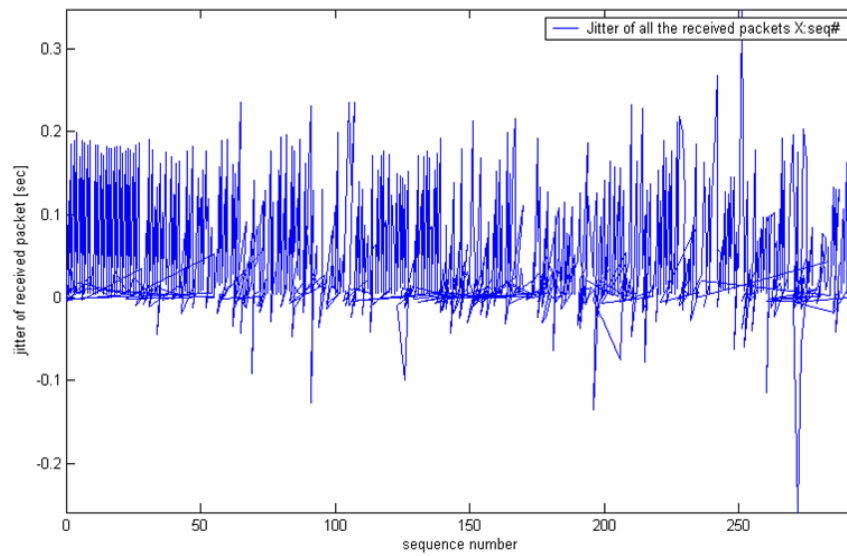
#### 4. Jitter

Figure 38 shows the jitter plots of transmitted and received traffic for WPAN and WLAN networks. It is observed that the packet jitter is low for both WLAN and WPAN networks.

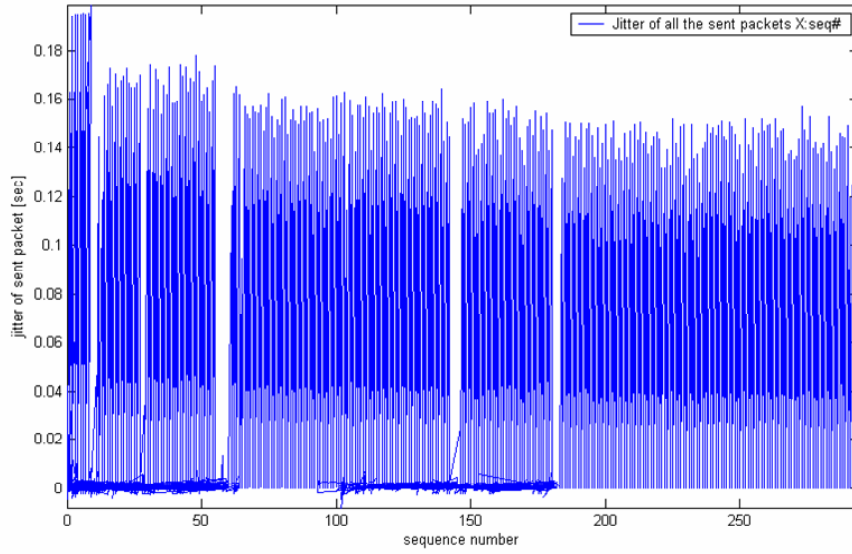
For the WPAN, the maximum jitter of sending packets is 200 ms and the maximum jitter of receiving packets is 320 ms. The average jitter of sending and receiving packets is approximately 8 ms. For WLAN, the maximum jitter of sending packets is 200 ms and the maximum jitter of receiving packets is also 200 ms. The average jitter of sending and receiving packets is approximately 5 ms.



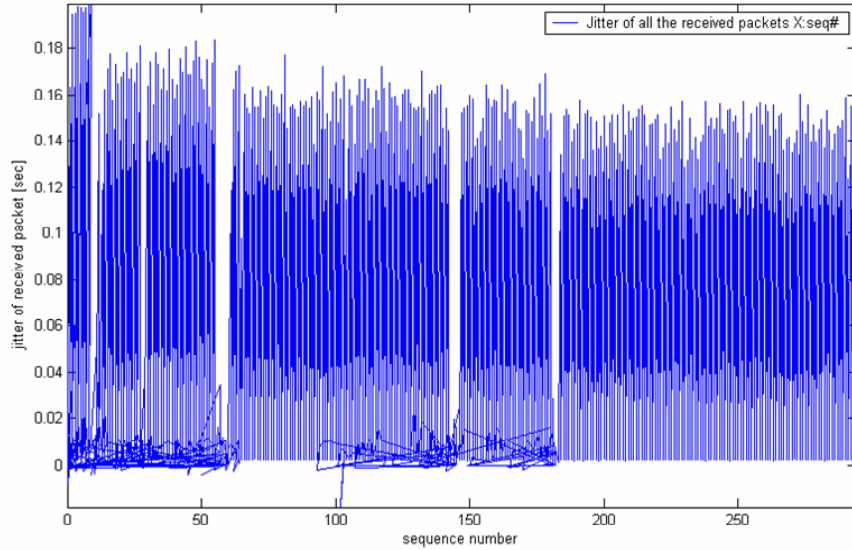
(a)



(b)



(c)



(d)

Figure 38. Jitter plot of: (a) all sent WPAN packets, (b) all received WPAN packets (c) all sent WLAN packets, (d) all received WLAN packets. NS-2 simulation of a 26-node network operating over an area of  $50 \times 50 \text{ m}^2$ .

The simulation results show that the wireless sensor network has a throughput between 20 kbps and 100 kbps, a low average delay of less than 10 ms and a low average jitter in the range of 5 ms to 10 ms. Assuming that the payload sent by each sensor to a

server for processing is 1 kByte, as has been implemented by Duckworth et al. [6], the required transmission time is approximately between 0.08 s and 0.4 s. After considering the processing time and other delays, the total delay can be approximated to be less than one second. This indicates that the wireless sensor network is suitable for implementation in fast-response counter-sniper applications.

This chapter has presented the simulation results of the hybrid SI/ML estimation method used in the two-step localization process for counter-sniper applications. Simulation results indicate that the proposed two-step localization method is suitable for counter-sniper applications. For example, twelve soldiers with two sensors each ( $6 \times 2 \times 2$ ) can detect a sniper 100 m away with an RMS error of 3 m, 8 m and 15 m for the  $X_s$ ,  $Y_s$  and  $Z_s$  values, respectively. Better accuracy can be obtained by increasing the number of sensors or by increasing the inter-sensor spacing. The NS-2 based simulation results indicate that both WPAN and WLAN networks are suitable for implementation in fast-response counter-sniper applications due to their high throughput, low delay and low jitter. The next chapter will conclude the thesis by summarizing the significant results and proposing possible future work.

## V. CONCLUSION

This thesis focused on source localization using wireless sensor networks. Wireless sensor nodes worn on soldiers or installed on vehicles can be deployed to form a distributed sensor array to locate the source of sniper fire. A two-step source localization process is proposed for counter-sniper applications: the time difference of arrival (TDOA) values are first determined using the generalized cross correlation (GCC) method and then the TDOA values are used by a hybrid spherical interpolation/maximum likelihood (SI/ML) estimation method to determine the shooter location. A simulation model has been developed in MATLAB to study the performance of the hybrid SI/ML estimation method. A wireless sensor network is simulated in NS-2 to study the network throughput, delay and jitter of the IEEE WPAN and WLAN networks.

### A. SIGNIFICANT RESULTS

The effects of number of sensor nodes, inter-sensor spacing, topology, noise, source-sensor distance, sensor node failure, and location perturbation on the location estimation performance of the hybrid SI/ML method have been studied through MATLAB simulation.

Simulation results show that the error variance can be reduced by increasing the number of sensor nodes or the inter-sensor spacing. To increase the estimation accuracy, the number of sensors as well as the inter-sensor spacing should be increased.

For the case of wearable sensors, the constraint of small inter-sensor spacing on the human body degrades the estimation accuracy. On the other hand, vehicular configuration providing larger vertical and horizontal inter-sensor spacing can help improve the estimation accuracy. We see that the configuration of a group of twelve soldiers or vehicles, with two wireless sensors per soldier or vehicle, is sufficient to accurately detect a sniper situated 100 m away with an RMS error of 3 m, 8 m and 15 m for the  $X_s$ ,  $Y_s$  and  $Z_s$  values, respectively. By using a longer range wireless network such as WLAN, the inter-sensor spacing can be increased and provides better estimate



accuracy to detect a sniper located farther. Simulation results also indicate that the sensor topology should be well represented in all three dimensions to obtain desirable resolution.

The source estimation accuracy is not adversely affected when encountering node failures or location perturbations. Results show that sensor node failures lead to a gradual degradation of accuracy and not a sudden total system failure. This demonstrates the advantage of using distributed wireless sensor networks to provide greater system robustness. It is observed that location perturbations do not adversely affect the location estimation. This illustrates the flexibility of the network configuration and demonstrates the suitability for potential field deployment.

Network simulation results based on the NS-2 package show that the wireless sensor network can support a throughput of between 20 kbps and 100 kbps, a low average delay of less than 10 ms, and a low average jitter in the range of 5 ms to 10 ms. These are suitable for fast response network-based sniper detection applications that require low delay and fast data exchange.

## **B. FUTURE WORK**

This thesis dealt with a single source scenario. In a future effort, the work reported here can be extended to multiple sources. Since the SI method is only applicable to a single source case, a different estimation method should be considered. Other source types, such as RF and seismic signals, can also be included in the simulation model.

We have seen that the SI method provided good initial values for the ML method. However, the SI method can introduce bias at low noise levels and affect the estimation accuracy of the ML method. Alternative estimation methods, such as linear interpolation (LI) [21] and cluster-based schemes [16], can be studied to replace the SI method in the two-step process. We also observed that the ML method failed to converge when the SI method produced noisy location estimates. Further study is required to analyze this behavior.

To improve the estimation accuracy of a nearby source, beamforming techniques can be applied as they generally provide a more accurate and robust performance in the near-field [17][22][23]. As discussed in this thesis, the proposed two-step process is

suitable for far-field applications. A combination of beamforming and the two-step process can be studied in a future effort to cover both near-field and far-field sources.

In this work, the two-step source localization process was simulated in MATLAB. This work can be extended by implementing the scheme in hardware using Crossbow motes and conducting field experiments. The measured results can be used to validate the simulated results provided in this thesis.

THIS PAGE INTENTIONALLY LEFT BLANK

## APPENDIX: MATLAB SOURCE CODE

This appendix lists the MATLAB source code used to study the performance of the Spherical Interpolation (SI) and Maximum Likelihood (ML) source localization estimation method.

```
% -----  
% Calculate Source Location based on Range Difference of Arrival (RDOA)  
% (1) Least Square Estimation - Spherical Interpolation (SI) Method  
% (2) Maximum Likelihood (ML) Method  
%  
% N sensors, 1 source  
% Using sensor 1 as reference i.e (x1=0, y1=0, z1=0)  
%  
% -----  
clear;  
% -----  
% Definition  
% -----  
nRun=100;      % number of Monte Carlo runs  
  
% uncomment one of them  
% bML=0;      % turn off ML calculation  
bML=1;      % turn on ML calculation  
  
% uncomment one of them  
perturb=0;      % turn off location perturbation  
% perturb=1;      % turn on location perturbation  
  
% -----  
% Actual source location (m) in Cartesian coordinates x, y and z  
% Note: For simplicity, we only varies y for our simulation  
% -----  
xs_src_actual=[0];  
  
% Varies the Y position (Choose 1)  
% -----  
ys_src_actual=[100]; %100 m  
zs_src_actual=[0];  
  
Rs_actual=sqrt(xs_src_actual.^2 + ys_src_actual.^2 + zs_src_actual.^2);  
% calculate corresponding range Rs  
bearing_actual=[xs_src_actual; ys_src_actual; xs_src_actual]/Rs_actual;  
% calculate corresponding bearing
```

```

% -----
% Actual sensor location (m) in Cartesian coordinates x, y and z
% Note: For simplicity, we only use integers and then multiply with
% a scaling factor to produce the actual coordinates.
% e.g. [5 10 15] = [1 2 3] * 5 ;
% -----

% Scale wrt to 1m (Choose 1)
%-----
scale_dist = 10 % 10 m

% (Choose 1 of the following sensor configuration for study)
%-----
% 12x2 sensors arranged 2 rows
% xi=[0 0 1 1 2 2 3 3 4 4 5 5 0 0 1 1 2 2 3 3 4 4 5 5].*scale_dist;
% yi=[0 1 0 1 0 1 0 1 0 1 0 1 0 1 0 1 0 1 0 1 0 1 0 1].*scale_dist;
% zi=[0 0 0 0 0 0 0 0 0 0 0 0 1 1 1 1 1 1 1 1 1 1 1 1].*1.0;
% Soldier configuration (each with 2 sensors). z= 1m apart vertically

temp=size(xi);
nSen=temp(1,2);          % number of sensor (>4)

noisestd=1;
if (perturb==1)
    randn('state',0);
    tmp1=randn(3, nSen);
    for i=1:2:nSen
        xi(i)= xi(i) + noisestd*tmp1(1,i);
        xi(i+1)= xi(i+1)+(noisestd+0.01)*tmp1(1,i); % less variance on the body
        yi(i)= yi(i) + noisestd*tmp1(2,i);
        yi(i+1)= yi(i+1)+(noisestd+0.01)*tmp1(2,i); % less variance on the body
    end
    zi=zi+0.01*tmp1(3,:); % less variance on the body
end

% RD noise (Choose 1)
% -----
Noise_Factor=0.001; % noise std = Std_Norm * (source distance). %
we expect bigger noise variance for larger distance.
Noise_Var=(Noise_Factor*Rs_actual)^2;

% -----
% Functions
% -----

```

```

% Random Process
% AWGN
    randn('state',0);
    noise = sqrt(Noise_Var)*randn(nRun, 1);
    %noise_mean = mean(noise, 2); % average along row

for k=1:nRun, % Monte Carlo Simulation

    Xi=[xi' yi' zi'];
    Di= sqrt ((xi-xs_src_actual).^2 + (yi-ys_src_actual).^2 + (zi-zs_src_actual).^2);
    Ri= sqrt ((xi).^2 + (yi).^2 + (zi).^2);

    locSen=[xi' yi' zi'];

    % using N sensors
    for i=1:nSen-1
        %d21=Di(2)-Di(1);
        %d31=Di(3)-Di(1);..
        %dn1=Di(n)-Di(1);
        %d=[d21;d31;...;dn1];
        d(i,1)=Di(i+1)-Di(1)+noise(k); %add noise to RD estimates

        % delta2=Ri(2)^2-d(1)^2;
        % delta3=Ri(3)^2-d(1)^2;...
        % deltan=Ri(n)^2-d(1)^2;
        % delta=[delta2;delta3;...deltan];
        delta(i,1)=Ri(i+1)^2-d(1)^2;

        % s2= [xi(2) yi(2) zi(2)];
        % s3= [xi(3) yi(3) zi(3)];...
        % sn= [xi(n) yi(n) zi(n)];
        % s=[s2;s3;...sn];
        s(i,:)= [xi(i+1) yi(i+1) zi(i+1)];

    end

    % define weight (positive definite, i.e., diagonal positive and symmetrical)
    w=eye(nSen-1); % set to identity matrix for unweighted case

    Sw=(s'*w*s)^(-1)*s'*w;
    Ps=s*Sw;
    Ps_ortho=eye(nSen-1)-Ps;

    %-----
    %SI method
    %-----

```

```

Rs_SI_cal=0.5*(d'*Ps_ortho*w*Ps_ortho*delta)/(d'*Ps_ortho*w*Ps_ortho*d);

% Calculate Xs for SI method
Xs_row_SI = 0.5*Sw*(delta-2*Rs_SI_cal*d);
Xs_SI(k,:)=Xs_row_SI';
Rs_SI(k,:)=sqrt(Xs_SI(k,1)^2 + Xs_SI(k,2)^2 + Xs_SI(k,3)^2);

bearing_SI(k,:)=Xs_SI(k,:)/Rs_SI(k,:);
% error_row= delta - 2*Rs_SI*d - 2*s*Xs_row_SI; %error
% error(k,:)=error_row';

% %-----
% % Maximum Likelihood Method
% % Objective function is contained in mlobjfun.m
% %-----
if (bML==1)
    x0 = Xs_SI(k,:); % As value obtained from SI as starting guess
    % x0 = [0 ys_src_actual 0]; % Starting guess
    options = optimset('LargeScale','off');

    % % LevenbergMarquardt
    options=optimset(options,'LevenbergMarquardt','on'); % LM
    % options=optimset(options, 'LevenbergMarquardt','off'); % Gauss Newton
    [x,resnorm,residual,exitflag,output]=
        lsqnonlin(@mlobjfun,x0,[],[],options,locSen,Noise_Var,d);
    Xs_ML(k,:)=x;
    Rs_ML(k,:)=sqrt(Xs_ML(k,1)^2+Xs_ML(k,2)^2+Xs_ML(k,3)^2);
    bearing_ML(k,:)=Xs_ML(k,:)/Rs_ML(k,:);
end

% -----
% Calculate bias (i.e., errors) for source location, range and bearing
% estimates
% -----

% Calculate mean
% -----
% SI
bias_Xs_SI(k,1)=Xs_SI(k,1)-xs_src_actual;
bias_Xs_SI(k,2)=Xs_SI(k,2)-ys_src_actual;
bias_Xs_SI(k,3)=Xs_SI(k,3)-zs_src_actual;

% ML
if (bML==1)

```

```

        bias_Xs_ML(k,1)=Xs_ML(k,1)-xs_src_actual;
        bias_Xs_ML(k,2)=Xs_ML(k,2)-ys_src_actual;
        bias_Xs_ML(k,3)=Xs_ML(k,3)-zs_src_actual;
    end
end

bias_Rs_SI = Rs_SI-Rs_actual;
bias_bearing_SI = 180/pi*acos(bearing_SI*bearing_actual);

if (bML==1)
    bias_Rs_ML=Rs_ML-Rs_actual;
    bias_bearing_ML = 180/pi*acos(bearing_ML*bearing_actual);
end

meanxs_SI=mean(bias_Xs_SI(:,1));
meanys_SI=mean(bias_Xs_SI(:,2));
meanzs_SI=mean(bias_Xs_SI(:,3));
meanrs_SI=mean(bias_Rs_SI);
meanbear_SI=mean(bias_bearing_SI);

vect_mean_SI=[meanxs_SI;meanys_SI;meanzs_SI;meanrs_SI;meanbear_SI];

%ML
if (bML==1)
    meanxs_ML=mean(bias_Xs_ML(:,1));
    meanys_ML=mean(bias_Xs_ML(:,2));
    meanzs_ML=mean(bias_Xs_ML(:,3));
    meanrs_ML=mean(bias_Rs_ML);
    meanbear_ML=mean(bias_bearing_ML);
    vect_mean_ML=[meanxs_ML;meanys_ML;meanzs_ML;meanrs_ML;
        meanbear_ML];
end

% Calculate Variance = E[(a - mean)^2]
% -----
varxs_SI=var(bias_Xs_SI(:,1));
varys_SI=var(bias_Xs_SI(:,2));
varzs_SI=var(bias_Xs_SI(:,3));
varrs_SI=var(bias_Rs_SI);
varbear_SI=var(bias_bearing_SI);

vect_var_SI=[varxs_SI;varys_SI;varzs_SI;varrs_SI;varbear_SI];

%ML
if (bML==1)

```



```

varxs_ML=var(bias_Xs_ML(:,1));
varys_ML=var(bias_Xs_ML(:,2));
varzs_ML=var(bias_Xs_ML(:,3));
varrs_ML=var(bias_Rs_ML);
varbear_ML=var(bias_bearing_ML);

vect_var_ML=[varxs_ML;varys_ML;varzs_ML;varrs_ML;varbear_ML];
end

% Calculate second moment (RMS)= sqrt {E[a^2]} = sqrt {mean^2 + variance}
% -----
rmsxs_SI=sqrt(mean(bias_Xs_SI(:,1)).^2+varxs_SI);
rmsys_SI=sqrt(mean(bias_Xs_SI(:,2)).^2+varys_SI);
rmszs_SI=sqrt(mean(bias_Xs_SI(:,3)).^2+varzs_SI);
rmsrs_SI=sqrt(mean(bias_Rs_SI).^2+varrs_SI);
rmsbear_SI=sqrt(mean(bias_bearing_SI).^2+varbear_SI);

vect_rms_SI=[rmsxs_SI;rmsys_SI;rmszs_SI;rmsrs_SI;rmsbear_SI];

%ML
if (bML==1)
rmsxs_ML=sqrt(mean(bias_Xs_ML(:,1)).^2+varxs_ML);
rmsys_ML=sqrt(mean(bias_Xs_ML(:,2)).^2+varys_ML);
rmszs_ML=sqrt(mean(bias_Xs_ML(:,3)).^2+varzs_ML);
rmsrs_ML=sqrt(mean(bias_Rs_ML).^2+varrs_ML);
rmsbear_ML=sqrt(mean(bias_bearing_ML).^2+varbear_ML);

vect_rms_ML=[rmsxs_ML;rmsys_ML;rmszs_ML;rmsrs_ML;rmsbear_ML];

end

% Calculate Cramer Rao Bound
%

cov_mat=Noise_Var.*(0.5*ones(length(d))+0.5*eye(length(d)));

for i=1:length(d)
    a1=[xs_src_actual-locSen(i+1,1) ys_src_actual-locSen(i+1,2)
        zs_src_actual-locSen(i+1,3)];

    a2=sqrt((xs_src_actual-locSen(i+1,1))^2+(ys_src_actual-locSen(i+1,2))^2
        +(zs_src_actual-locSen(i+1,3))^2);
    b1=[xs_src_actual-locSen(1,1) ys_src_actual-locSen(1,2)
        zs_src_actual-locSen(1,3)];
    b2=sqrt((xs_src_actual-locSen(1,1))^2+(ys_src_actual-locSen(1,2))^2

```

```

        +(zs_src_actual-locSen(1,3))^2);
    jacobian(i,:)= (a1/a2)-(b1/b2);
end

fisher=jacobian'*inv(cov_mat)*jacobian;

crlb= trace(fisher^-1); % compare with MSE of Rs

% -----
% Generate Plots
% -----

% hfig1=figure;
if (bML==1)
plot(xi, yi,'kv', xs_src_actual, ys_src_actual, 'k^', Xs_SI(:,1), Xs_SI(:,2),
'ko',Xs_ML(:,1), Xs_ML(:,2), 'kd'); % plot both SI and ML
else
plot(xi, yi,'kv', xs_src_actual, ys_src_actual, 'k^', Xs_SI(:,1), Xs_SI(:,2), 'ko');
% plot just SI only
end

title('Sensor and Source Location');
str1=sprintf('[Xs, Ys, Zs, Rs, Bearing], Noise Std = %s*Rs',Noise_Factor);
str2=sprintf('SI Method');
str3=sprintf('RMS = [%s, %s, %s, %s, %s]', rmsxs_SI, rmsys_SI, rmszs_SI,
rmsrs_SI, rmsbear_SI);
str4=sprintf('Mean = [%s, %s, %s, %s, %s]', meanxs_SI, meanys_SI, meanzs_SI,
meanrs_SI, meanbear_SI);
str5=sprintf('Variance = [%s, %s, %s, %s, %s]', varxs_SI, varys_SI, varzs_SI,
varrs_SI, varbear_SI);
if (bML==1)
str6=sprintf('ML Method');
str7=sprintf('RMS = [%s, %s, %s, %s, %s]', rmsxs_ML, rmsys_ML, rmszs_ML,
rmsrs_ML, rmsbear_ML);
str8=sprintf('Mean = [%s, %s, %s, %s, %s]', meanxs_ML, meanys_ML,
meanzs_ML, meanrs_ML, meanbear_ML);
str9=sprintf('Variance = [%s, %s, %s, %s, %s]', varxs_ML, varys_ML,
varzs_ML, varrs_ML, varbear_ML);
str=sprintf('%s \n%s \n%s \n%s \n%s \n%s \n%s \n%s \n%s', str1, str2, str3, str4,
str5, str6, str7, str8, str9);
legend('sensor location', 'actual source location ', 'calculated source location
(SI)', 'calculated source location (ML)');
else
str=sprintf('%s \n%s \n%s \n%s \n%s \n%s \n%s \n%s \n%s', str1, str2, str3, str4,
str5);
legend('sensor location', 'actual source location', 'calculated source location (SI)');

```

```

end

text(scale_dist/10,ys_src_actual,str);
xlabel('Distance (metres) in X direction');
ylabel('Distance (metres) in Y direction');

% generate results output files
fid = fopen('results.txt','w');

for k=1:nRun,
    fprintf(fid,'%e\t%e\t%e\t%e\t%e\n',bias_Xs_SI(k,1),bias_Xs_SI(k,2),
        bias_Xs_SI(k,3), bias_Rs_SI(k), bias_bearing_SI(k));
end
fprintf(fid,'\n%e\t %e\t %e\t %e\t %e\n', meanxs_SI, meanys_SI, meansz_SI,
    meanrs_SI, meanbear_SI);
fprintf(fid,'%e\t %e\t %e\t %e\t %e\n', varxs_SI, varys_SI, varzs_SI, varrs_SI,
    varbear_SI);
fprintf(fid,'%e\t %e\t %e\t %e\t %e\n', rmsxs_SI, rmsys_SI, rmszs_SI, rmsrs_SI,
    rmsbear_SI);

fclose(fid);

```

## LIST OF REFERENCES

- [1] M. Haenggi, "Opportunities and Challenges in Wireless Sensor Networks," Handbook of Sensor Networks: Compact Wireless and Wired Sensing Systems, Ch. 1, CRC Press, 2005.
- [2] W. Su, E. Cayirci and Ö. Akan, "Overview of Communication Protocols for Sensor Networks," Handbook of Sensor Networks: Compact Wireless and Wired Sensing Systems, Ch. 16, CRC Press, 2005
- [3] R. Stoughton, "Measurements of Small Caliber Ballistic Shock Waves in Air," JASA 102 (2), Pt. 1, pp. 781-787, August 1997.
- [4] G. Simon, M. Maroti, A. Ledeczki, G. Balogh, B. Kusy, A. Nadas, G. Pap, J. Sallai and K. Frampton, "Sensor Network-based Countersniper System," ACM Second International Conference on Embedded Networked Sensor Systems (SenSys 04), pp. 1-12, November 2004.
- [5] M. Pauli, M. C. Ertem and E. Heidhausen, "Quick Response Airborne Deployment of Viper Muzzle Flash Detection and Location System During DC Sniper Attacks," Proceedings of the 32nd Applied Imagery Pattern Recognition Workshop (AIPR'03), pp. 221-228, October 2003.
- [6] G. L. Duckworth, J. E. Barger, S. H. Carlson, D. C. Gilbert, M. L. Knack, J. Korn and R. J. Mullen, "Fixed and wearable acoustic counter-sniper systems for law enforcement," Proceedings of SPIE Vol. 3577, Sensors, C3I, Information, and Training Technologies for Law Enforcement, pp. 210-230, November 1998.
- [7] M. Yarvis and W. Ye, "Tiered Architectures in Sensor Networks," Handbook of Sensor Networks: Compact Wireless and Wired Sensing Systems, Ch. 13, CRC Press, 2005.
- [8] IEEE Standard 802.15.4-2003, "Specific requirements Part 15.4: Wireless Medium Access Control (MAC) and Physical Layer (PHY) Specifications for Low Rate Wireless Personal Area Networks (LR-WPANs)," IEEE, 2003.
- [9] Zigbee Alliance, <http://www.zigbee.org>. Last accessed 20 Apr 2006.
- [10] J. DiBiase, H. Silverman and M. Brandstein, "Robust localization in reverberant rooms," Microphone Arrays: Signal Processing Techniques and Applications, Ch. 8, pp. 157-180, Springer, 2001.
- [11] J. M. Peterson and C. Kyriakakis, "Hybrid Algorithm for Robust, Real-time Source Localization in Reverberant Environments," International Conference on Acoustics, Speech and Signal Processing, Vol. 4, pp. 1053-1056, March 2005.

- [12] C. H. Knapp and G. C. Carter, "The generalized correlation method for estimation of time delay," *IEEE Transaction on Acoustics, Speech, and Signal Processing*, Vol. ASSP-24, No. 4, pp. 320-327, August 1976.
- [13] J. O. Smith and J. S. Abel, "Closed-Form Least-Squares Source Location Estimation from Range-Difference Measurements," *IEEE Transaction on Acoustics, Speech, and Signal Processing*, Vol. ASSP-35, No. 12, pp. 1661-1669, December 1987.
- [14] T. Ajdler, I. Kozintsev, R. Lienhart and M. Vetterli, "Acoustic source localization in distributed sensor networks," *Proceedings of the Thirty-Eighth Asilomar Conference on Signals, Systems and Computers*, Vol. 2, pp. 1328-1332, November 2004.
- [15] D. Marquardt, "An Algorithm for Least-Squares Estimation of Nonlinear Parameters," *SIAM J. Appl. Math.* Vol. 11, No. 2, pp. 431-441, June 1963.
- [16] K. Dogancay, "Emitter Localization using Clustering-Based Bearing Association," *IEEE Transactions on Aerospace and Electronic Systems*, Vol. 42, No. 2, pp. 525-536, April 2005.
- [17] J. C. Chen, K. Yao, and R. E. Hudson, "Source Localization and Beamforming," *IEEE Signal Processing Magazine*, pp. 30-39, March 2002.
- [18] D. Johnson and D. Dudgeon, "Array Signal Processing: Concepts and Techniques," Prentice Hall, 1993.
- [19] J. Zheng and M. J. Lee, "A Comprehensive Performance Study of IEEE 802.15.4," *IEEE Press Book*, 2004.
- [20] E. M. Royer and C. E. Perkins. "An Implementation Study of the AODV Routing Protocol," *Proceedings of the IEEE Wireless Communications and Networking Conference*, Chicago, IL, Vol. 3, pp. 1003-1008, September 2000.
- [21] M. Branstein, J. Adcock and H. Silverman, "A Closed-Form Location Estimator for Use with Room Environment Microphone Arrays," *IEEE Transaction on Speech and Audio Processing*, Vol. 5, No. 1, pp. 45-50, January 1997.
- [22] B. Mungamuru and P. Aarabi, "Enhanced Sound Localization," *IEEE Transactions on Systems, Man, and Cybernetics—Part B: Cybernetics*, Vol. 34, No. 3, pp. 1526-1540, June 2004.
- [23] B. D. Van Veen and K. M. Buckley. "Beamforming: A Versatile Approach to Spatial Filtering," *IEEE Acoustics, Speech, and Signal Processing Magazine*, pp. 4-24, April 1988.

## INITIAL DISTRIBUTION LIST

1. Defense Technical Information Center  
Ft. Belvoir, Virginia
2. Dudley Knox Library  
Naval Postgraduate School  
Monterey, California
3. Professor Jeffrey Knorr, Chairman, Code EC  
Department of Electrical and Computer Engineering  
Naval Postgraduate School  
Monterey, California
4. Professor Murali Tummala  
Department of Electrical and Computer Engineering  
Naval Postgraduate School  
Monterey, California
5. Professor John C. McEachen  
Department of Electrical and Computer Engineering  
Naval Postgraduate School  
Monterey, California
6. Stephen Tan Kok Sin  
Defence Science & Technology Agency  
Singapore
7. USSOCOM  
MacDill AFB, Florida